Physics – Uspekhi **65** (6) 567 – 596 (2022)

REVIEWS OF TOPICAL PROBLEMS

PACS numbers: 68.60.Bs, 68.65.Pq, 72.80.Vp, **73.40. – c,** 77.65.Ly

Straintronics of 2D inorganic materials for electronic and optical applications

I V Antonova

DOI: https://doi.org/10.3367/UFNe.2021.05.038984

Contents

Abstract. Straintronics, being a platform for creating new-generation information processing devices and a physical basis for the development of flexible electronics using two-dimensional (2D) inorganic materials, is currently a rapidly developing field of nanoelectronics. An attractive feature of the new family of 2D crystals is their capacity for deformation and stretching. The use of deformations can lead to remarkable changes in the electronic properties of 2D materials and van der Waals heterostructures based on them and to nonconventional technological and engineering solutions. Deformation engineering as an avenue to explore the potential to adjust the physical properties of materials by controlling elastic deformation fields is ideal for implementation precisely in atomically thin materials and structures.

Keywords: straintronics, graphene, 2D materials, heterostructures, mechanical properties, band gap, electrical properties, photoluminescence, light scattering, light absorption, adjustment of optical properties, local deformations, corrugated monolayers, atomic adsorption, potential applications

I V Antonova
Rzhanov Institute of Semiconductor Physics,
Siberian Branch of the Russian Academy of Sciences,
prosp. Lavrent'eva 13, 630090 Novosibirsk, Russian Federation
E-mail: antonova@isp.nsc.ru

Received 24 November 2020, revised 16 April 2021
Uspekhi Fizicheskikh Nauk **192** (6) 609 – 641 (2022)
Translated by S Alekseev

1. Introduction

Straintronics is a relatively new field in the physics of condensed matter, which uses the methods of deformation engineering and physical effects induced by mechanical deformations in solids to construct new-generation devices for information, sensor, and energy-saving technologies [1]. At present, two main branches of straintronics can be identified: straintronics of magnetic materials and straintronics of two-dimensional (2D) and semiconducting crystals. The focus in review [1] was on magnetic and magnetoelectric materials, such as the nickel films $BiFeO_3$ and $Co_{40}Fe_{40}B_{20}$, $Ni_{75}Fe_{25}$ permalloy films, and other materials and composites. Magnetic materials exhibit a wide range of effects associated with deformations and interactions between different subsystems in crystals (magnetoresistive, piezoresistive, and other effects; see, e.g., [1–4]). An advantage of magnetic straintronic devices is their energy independence, i.e., the ability to save the state of the device when the voltage is switched off [5]. But most importantly, it is assumed that just the magnetic straintronics can allow ultra-low power consumption to be realized in switching over storage devices (below 1 aJ), so as to approach the fundamental thermodynamic limits [6, 7]. We note that this expectation is valid not only for magnetic materials but also for the entire class of memristors made of 2D materials.

The second branch of straintronics deals with effects such as alterations in the band structure of 2D materials and in the electrical (transport), optical, magnetic, and other properties of materials to create new-generation nanoelectronic devices.

In this review, we consider the effects associated with the effect of external and internal deformations on the properties of 2D materials such as graphene, its compounds, transition material dichalcogenides, boron nitride, and monolayer semiconductors (silicene, germanene, phosphorene, etc.). In such materials, the transition to monolayers dramatically changes many of their properties, including mechanical ones; the materials become flexible and capable of stretching [8].

Deformation engineering is one of the key approaches to improve the performance and functional properties of present-day silicon-based technologies [9]. For example, the creation of strained layers of bulk semiconductors allows increasing the mobility of carriers in stretched silicon grown on an SiGe layer in order to create deformations in silicon due to a larger (by 4%) lattice constant of germanium [10]. Mechanical stress can reduce the effective mass of carriers, which also leads to an increase in their mobility. In stretched silicon on an SiGe layer with a $\sim 30\%$ germanium content, the gain can reach maximum values of $\sim 80\%$ for electrons and $\sim 70\%$ for holes.

A novelty in modern straintronics is the transition to the use of monolayer materials and heterostructures based on them, which significantly changes the mechanical properties and expands the potential for using materials for flexible electronics. A significant change in the interatomic distance and crystal lattice symmetry under large elastic deformations can lead to the appearance of unusual mechanical, thermal, optical, electrical, magnetic, and other properties. In addition, as a result of the development of technologies for the transfer of thin films and monolayers in combination with their growth, it has become possible to obtain new types of heterostructures, unattainable by other methods. Such heterostructures, on the one hand, open new horizons for applications and, on the other hand, show unexpected effects associated with deformations. For example, MoS_2/WS_2 heterostructures grown by chemical vapor deposition (CVD) under a stretching deformation of $\sim 1.2\%$ showed the possibility of 'decoupling' the monolayers in the heterostructure [11].

With the use of straintronic approaches, the research subjects underlying the development of flexible electronics are currently being shaped. Flexible electronics includes a class of different electronic devices that can be subjected to mechanical stress (can be bent, twisted, compressed, or stretched) without compromising their functional properties. It is expected that flexible electronics in the near future will allow creating all kinds of high-tech accessories, touch screens, sensors, devices for communication, and the Internet of things and will have a wide range of applications in medicine [12–15]. Currently, it is already possible to identify avenues for development, such as stretchable, foldable, and wearable electronics [16, 17]. Flexible electronics now have a pronounced 'household' focus: wearable high-tech accessories are used daily in everyday life by millions of people, including, in particular, miniaturized devices for monitoring a person's condition (pulse rate, blood pressure, temperature, etc.). Wearable accessories are usually synchronized with smartphones or desktop computers. This allows not only tracking information about a person's condition but also storing and analyzing it with dedicated applications. Flexible electronic devices were initially based on organic materials, which have relatively low stability and conductivity [18]. The advent of 2D inorganic materials and the development of technologies for their production gave a powerful impetus to the development of straintronics and flexible electronics based on such materials [19, 20].

Recently, a large number of papers have been published on the study of the effect of deformations on the properties of specific device structures made of graphene and other 2D materials. Most often, these studies deal with bends, and less often, with the effect of stretching, twisting, and other types of deformation. We make a special note of a flood of studies aimed at developing sensors for medical applications, primarily portable devices for monitoring the state of human health (see, e.g., [21, 22]). In such studies, to ensure the flexibility and resistance of structures and contact paths to twisting, a special flexuous configuration is used, which is especially relevant for sensors worn on the skin or applied to textiles. For example, in [23], we demonstrated the stability of the functional properties of humidity sensors of a zigzag shape made of graphene-based composite layers against deformations up to $\pm 1.5\%$ (bending radius down to 3 mm).

Deformations in graphene and other 2D materials can occur due to natural causes [24]. For example, graphene on a substrate usually experiences moderate deformation due to the graphene–substrate lattice mismatch [25] or the substrate surface topography [26]. On the other hand, deformations lead to the mechanical instability of graphene: only less than 0.1% of compressive deformation can be applied to a micrometer-size graphene structure without changing the layer configuration [27]. Compressive deformation must inevitably lead to the formation of ripples or folds [27–29]. In addition, there is an inherent edge stress along the edges of graphene, which causes mechanical twisting of the edges. And, of course, it is possible to deliberately induce deformations and control them in graphene using various methods.

Uniaxial deformation can be caused by bending a flexible substrate on which graphene is deposited without slipping [30, 31]. Biaxial deformation can be produced by three typical methods. The first is to use the tip of an atomic-force microscope (AFM) to deform graphene deposited over a hole formed in the substrate [32]. In the second approach, graphene is transferred to a piezoelectric substrate, which is compressed or stretched in a controlled manner, thereby subjecting the graphene to a uniform biaxial deformation [33]. The third method relies on the thermal expansion mismatch between graphene and the substrate to produce deformation in graphene [34]. Given the negative thermal expansion coefficient of graphene, a substrate with a positive thermal expansion coefficient can be chosen (e.g., SiO_2) [35]. When the substrate is subsequently heated or cooled, graphene experiences stretching or compressive biaxial deformation.

In this review, we consider the available knowledge on the mechanical properties of 2D inorganic materials and heterostructures based on them, on the possibilities of using straintronics to create new materials and structures with unusual properties, and on basic approaches to the development of flexible electronics. Graphene is the strongest of the studied 2D materials, capable of withstanding a reversible elastic stretching deformation exceeding 25% [32], which suggests interesting prospects for tuning the properties of graphene by deformation, thereby maintaining steady progress in straintronics [24]. For comparison, silicon usually fails at a deformation level of $\sim 1.5\%$ [36]. We first consider the effect of deformation on the Raman spectra and the electronic structure of graphene and other 2D materials.

Next, we discuss examples of introducing and using local deformations to create artificial atoms and control tunneling currents, conduction, and charge carrier mobility. We consider alterations in the properties of materials resulting from a combination of deformation with a rotation of layers in bilayer structures and the prospects for using deformation for the controlled self-assembly of foreign atoms on the surface of graphene. We conclude with a description of the deformation effects for vertical heterostructures. On the whole, we must note the significant predominance of theoretical over experimental work [37–39]. For example, a large number of theoretical studies demonstrate the appearance of a band gap in graphene under various types of deformation, but experimental studies confirming this conclusion are currently virtually absent.

2. Changes in mechanical properties under the transition to 2D materials

The mechanical properties of graphene have been studied quite thoroughly. Defect-free graphene has extremely high mechanical characteristics, such as a strength of ≈ 130 GPa, maximum elastic deformation of $\approx 25\%$, and Young's modulus $E^{2D} \approx 1000$ GPa [40].

Graphene is usually regarded as a continuous membrane ~ 0.335 nm in thickness. Under small deformations, graphene can be considered an isotropic linear elastic material, which can be described by Young's modulus E (a quantity characterizing the ability of a substance to resist longitudinal stretching or compression under elastic deformation) and Poisson's ratio v (the ratio of relative transverse compression to relative longitudinal stretching). Under large deformations, the dependence of stress σ on strain ε is described by two parameters, the second-order linear elastic modulus E and the third-order nonlinear elastic modulus D [32, 40],

$$\sigma = E\varepsilon + D\varepsilon^2 , \qquad (1)$$

where $D < 0$, and therefore the presence of a second-order term leads to a decrease in stiffness upon greater stretching. The strength of the material can be determined by the maximum value σ_{max}, which must solve the equation $\partial\sigma/\partial\varepsilon = 0$. The calculated strength and corresponding strain are then expressed as

$$\sigma_{max} = -\frac{E^2}{4D} , \qquad \varepsilon_{max} = -\frac{E}{2D} . \qquad (2)$$

If the strain exceeds ε_{max}, graphene is then considered a brittle material, and the graphene lattice is unstable and can break under such strains.

Theoretical studies often show a decrease in Young's modulus under the transition from graphene to multigraphene (see Table 1 and also [41]). For example, the mechanical properties of multilayer graphene consisting of 2 to 7 atomic planes and of bulk graphite were studied theoretically by molecular dynamics in [42]. It was found that, with an increase in the number of layers, the coupling strength of adjacent layers increases, which reduces the elastic modulus and tensile strength. If the number of layers exceeds four (Fig. 1a), then, according to [42], the multilayer material becomes brittle. However, the experimental values of Young's modulus for MoS_2 showed a weaker dependence of this parameter on the layer thickness; a stronger increase in Young's modulus is exhibited by multigraphene of fewer than 6 monolayers in thickness, while Young's modulus does not change for hexagonal boron nitride h-BN (Fig. 1b) [43]. The measurements were carried out on blisters (bubbles formed during the deposition of 2D materials on the required substrates) using probe spectroscopy. In [38], a theory was proposed that provides a better description of the actual dependence of Young's modulus on thickness. In addition to graphene (Fig. 1c), we also consider two-layer graphene structures with A–A packing and with one third of the parallel bonds replaced with carbon dimers.

Table 1. Elastic modulus E^{2D}, Young's modulus $E = E^{2D}/h$, where h is the thickness of a 2D material, stretching deformation σ^{2D}, limit strength σ_{max}, maximum strain ε_{max}, Poisson's ratio v.

Material	E^{2D}, N m^{-1}	E, GPa	σ^{2D}, N m^{-1} (GPA)	σ_{max}, N m^{-1}	ε_{max}	v	Reference
Graphite	342					0.165	[38]
Graphite		11	2 – 12				[45]
Graphene (theory) (0.335 nm)	285 – 384	850 – 1146			0.25	0.14 – 0.33	[38]
Graphene (theory) (0.335 nm)	305 – 415	910 – 1240		26 – 40	0.14 – 0.33	0.15 – 0.45	[41]
Graphene flakes	340	1025	130 (388)	42	0.20		[32]*
Graphene flakes	350	1045					[52]*
CVD graphene	34 – 39	~ 100					[50]*
Reduced graphene oxide (RGO)	~ 84	~ 250					[53]*
Graphene flakes	100			15			[54]*
Hydrogenated graphene	248	740					[55]
h-BN (0.42 nm)	279	665	21	—		0.22	[56]
h-BN (0.42 nm)	256 – 407	610 – 970	120 – 165				[57]
$MoSe_2$ (0.65 nm)		176 – 179	13 – 23		0.16 – 0.29	0.33	[58]
WS_2 (0.65 nm)	132 – 177	272			0.15		[59]*
Phosphorene (0.5 nm)	88 – 332	44 – 166	8 – 18		0.11 – 0.48	0.17 – 0.62	[37]
Silicene (0.4 nm)	142 – 155	57 – 62	6.0 – 7.2		0.17 – 0.19	0.29 – 0.33	[37]
Germanene (0.32 nm)	134 – 137	43 – 44	4.1 – 4.7		0.20	0.29 – 0.35	[37]
Stanene (0.35 nm)	69 – 71	24 – 25	2.2 – 2.6		0.17 – 0.18	0.36 – 0.42	[37]
MoS_2/WS_2	314	348			0.25		[59]*
MoS_2/graphene	467	520			0.35		[59]*

* Experimental study

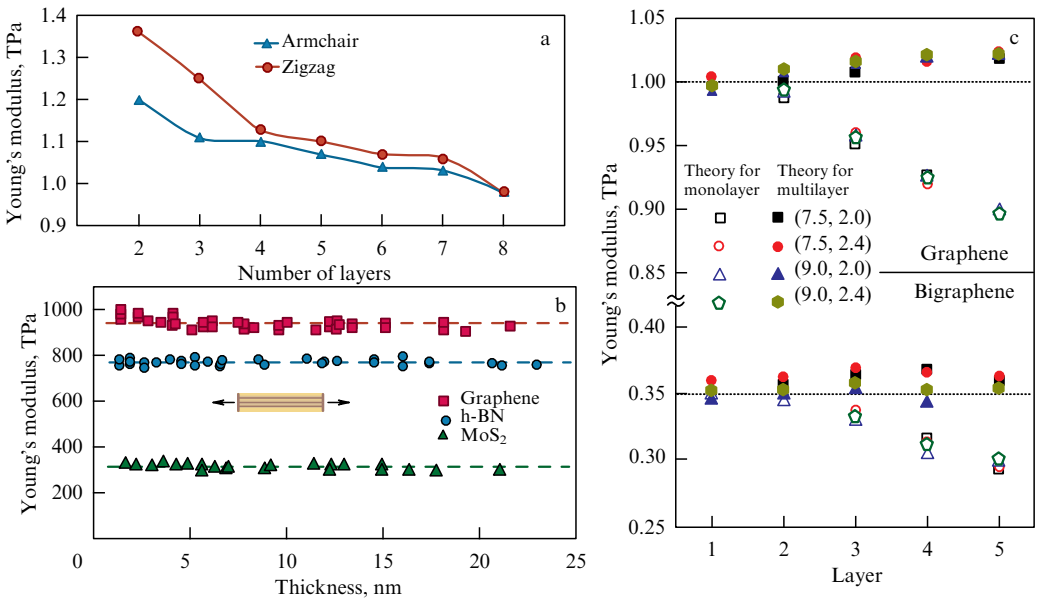

Figure 1. (a) Dependence of Young's modulus on the number of layers according to data in [42]. (b) Experimental studies of dependences of Young's modulus for graphene, hexagonal boron nitride h-BN, and MoS_2 on the film thickness [43]. (c) Young's modulus for graphene and bigraphene. Filled symbols and open symbols are results obtained for the respective multilayer and single-layer models proposed in [38]. Parameters in the figure: size of the considered particle and diameter of the tip, expressed in nm, are shown in parentheses. One third of the parallel bonds in graphene and two-layer graphene structures are replaced with carbon dimers.

Another important parameter of the mechanical properties of graphene is the maximum strength of the material under deformation; for graphene, this parameter is theoretically equal to 130 N m^{-1} (or 388 GPa, if expressed in volumetric units), while for graphite the maximum strength under different types of deformations is 10–30 MPa [44]. For graphite foil, depending on the doping level, the maximum tensile strength is 2–12 MPa [45]. According to the data in [46], the maximum strength of polycrystalline CVD-grown graphene with well-crosslinked grains is 34–39 N m^{-1} ($\sim$ 100 GPa). Thus, despite the presence of grain boundaries and defects, CVD graphene has a relatively high strength and can act as a strong large-area material for flexible electronics. This is a typical example where the mechanical properties of 2D materials differ significantly from those of a bulk material, allowing the use of monolayers as a flexible, stretchable material. We note that such materials include graphene compounds [47], transition-metal dichalcogenides [48], and other 2D materials.

An exception is hexagonal boron nitride, whose properties remain practically unchanged in moving to monolayers [17, 49]. Moreover, the coupling between the layers of this material is relatively strong, which complicates the preparation of h-BN monolayers. Usually, to create structures based on graphene, films of hexagonal boron nitride are used as dielectric layers [50]. This provides a high mobility of charge carriers in graphene due to a hexagonal structure similar to graphene and the low charge. But manufacturing flexible electronic devices using h-BN has significant limitations. Transistors that use h-BN as a substrate for graphene (transistor channel) fail at $\sim$ 1% deformation [51]. In transistors printed using an h-BN suspension, the characteristics change by orders of magnitude already with small bends in the structures [17].

The most promising flexible dielectric material is fluorinated graphene [60–62]. Fluorinated graphene is stable up to 450 °C, has good flexibility, and allows obtaining thin layers from a suspension with a low surface relief, low leakage currents, and ultra-low charge, but has a dielectric constant $\varepsilon \sim 1.2$. The dielectric constant can be increased to $\sim$ 3.5 by using a two-layer dielectric made of graphene oxide and fluorinated graphene [63].

3. Effect of deformation on the structural properties of graphene and its compounds

3.1 Deformation testing using Raman spectroscopy

Raman spectroscopy is a key diagnostic tool for graphene and other 2D materials.

The Raman spectra of single-layer graphene have two main peaks: the G mode at $\sim$ 1580 cm^{-1} and the 2D mode at $\sim$ 2700 cm^{-1}. The dependence of the position and width of peaks in the graphene Raman spectra on the magnitude of deformation has been studied well [64]. For example, the authors of [65] studied the change in the Raman spectra of graphene deposited on a flexible substrate under the action of stretching deformations up to 0.8% (Fig. 2). The Raman spectra of deformed graphene exhibit shifts of the respective 2D and G bands by 27.8 and 14.2 cm^{-1}/%. The cause of the shift is the elongation of carbon-carbon bonds under stretching.

Under uniaxial deformation, the splitting of the G peak into two bands can be observed (measurements done with polarized incident light); these are shown in Fig. 3 as G^+ and G^- in accordance with their energies [66]. It has been found that the relative intensities of the G^+ and G^- peaks strongly depend on the incident light polarization direction; this can be used to determine the angle between the deformation direction and the crystallographic orientation of graphene. The G-band splits due to a decrease in graphene symmetry under uniaxial stretching. For undeformed graphene, the G band arises from the doubly degenerate phonon mode E_{2g} at the center of the Brillouin zone. The 2D peak also splits into

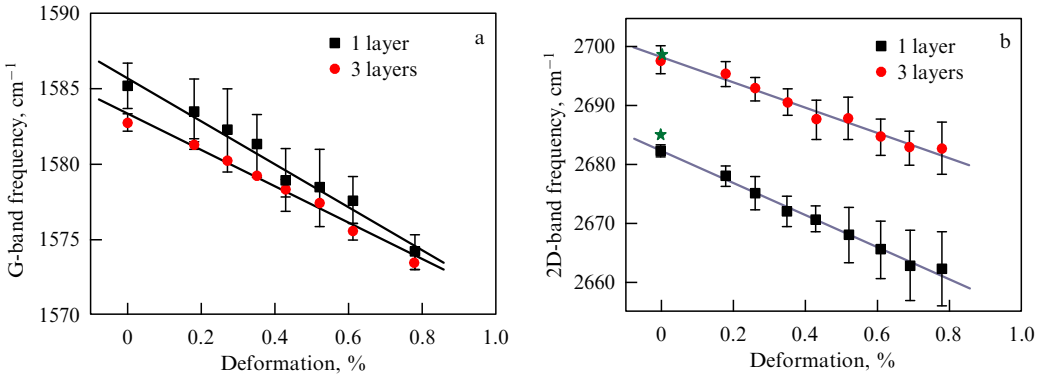

Figure 2. (Color online.) (a) Frequency of the G band observed in single-layer (black squares) and three-layer (red dots) graphene under uniaxial stretching. Slope is 14.2 cm^{-1}/% for single-layer graphene and 12.1 cm^{-1}/% for three-layer graphene. (b) Frequency of the 2D peak observed in single-layer (black squares) and three-layer (red dots) graphene under stretching deformation. Green points (stars) are frequencies of undeformed graphene. Slope is 27.7 cm^{-1}/% for single-layer and 21.9 cm^{-1}/% for three-layer graphene [65].

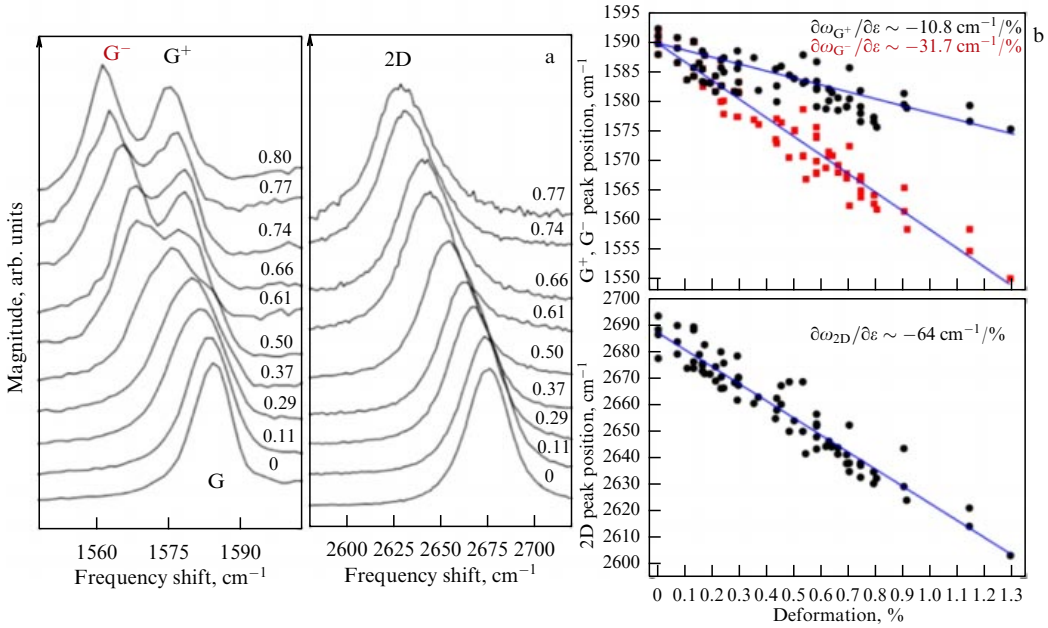

Figure 3. (a) G and 2D peaks depending on the uniaxial deformation of graphene. Strain value is indicated on the spectra as a parameter. (b) Position of G^+, G^-, and 2D peaks vs. uniaxial deformation [66].

two peaks, $2D^+$ and $2D^-$, under uniaxial deformation [67, 68]. The magnitude of the frequency shift depends on the direction of the applied deformation. It was shown in [67] for a graphene sample extended along the armchair direction that the respective $2D^+$ and $2D^-$ shear rates are -44.1 and -63.1 cm^{-1}/%, while for a graphene sample stretched along the zigzag direction, these rates are -26.0 and -67.8 cm^{-1}/%. Similar dependences of shear rates on the direction of deformation for the $2D^+$ ($2D^-$) peak were found in other studies (see, e.g., [68]), although the values of shear rates determined by different groups differ. The physical cause of the splitting of the peak is the shift of Dirac cones from the K and K′ points in opposite directions under uniaxial stretching, which leads to the appearance of two types of phonon scattering paths.

The effect of biaxial deformation on Raman spectra was also studied experimentally and theoretically [33, 69]. Under biaxial deformation, all symmetries of graphene are preserved, and hence the G and 2D bands do not split, and redshifts are observed.

The study of graphene deposited onto an SiO_2/Si substrate, using a detailed analysis of changes in the position of G and 2D modes in the Raman spectra, allowed separating two main factors of the influence of the substrate on graphene leading to the mode shift: the initial deformations of graphene by SiO_2/Si and its additional doping with holes, which usually occurs during heat treatment [70]. Figure 4 shows the positions of the G and 2D peaks in the Raman spectra, including the dependences on deformation and the layer-wise concentration of carriers. The parameter used in the calculations, the sensitivity of the uniaxial G-mode deformation $\Delta\omega_G/\Delta\varepsilon = -23.5$ cm^{-1}/%, was calculated from the data in [67] taking the splitting of the G-mode and the random orientation of the deformation with respect to the graphene crystal lattice into account. As a result, it was shown that in most cases, the original

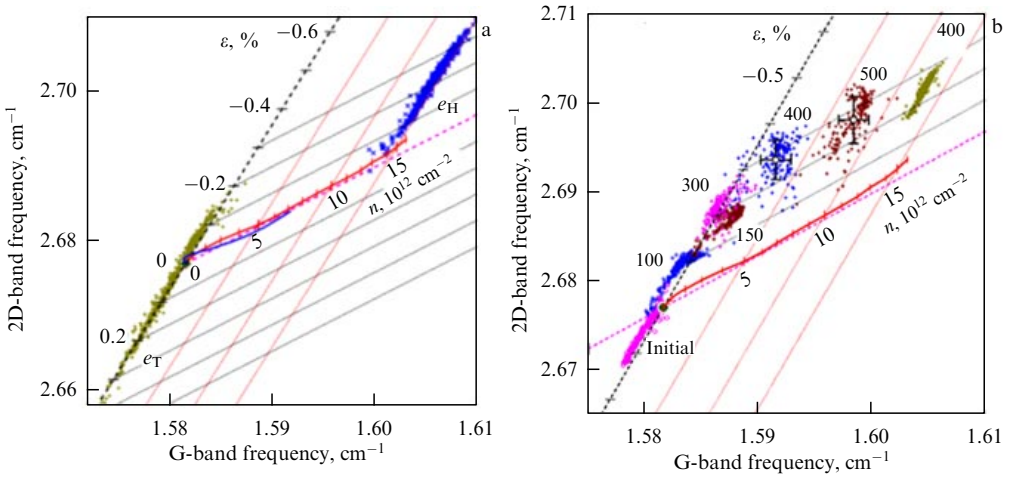

Figure 4. (Color online.) (a) Theoretical and experimental dependences of frequencies of 2D and G peaks observed under graphene deformation and layer-wise concentration of carriers in the range of 0–1.6 × 10^{13} cm^{-2} according to Raman scattering data for the initial structure (+) and the structure annealed at 400 °C (×). Red lines correspond to the marked values of the carrier concentration, black lines show the uniaxial strain ε in the range from −0.6 to 0.3%. (b) Changes in frequencies under successive annealing of the structure. Horizontal and vertical errors are also shown for $T = 400$ and 500 °C [70].

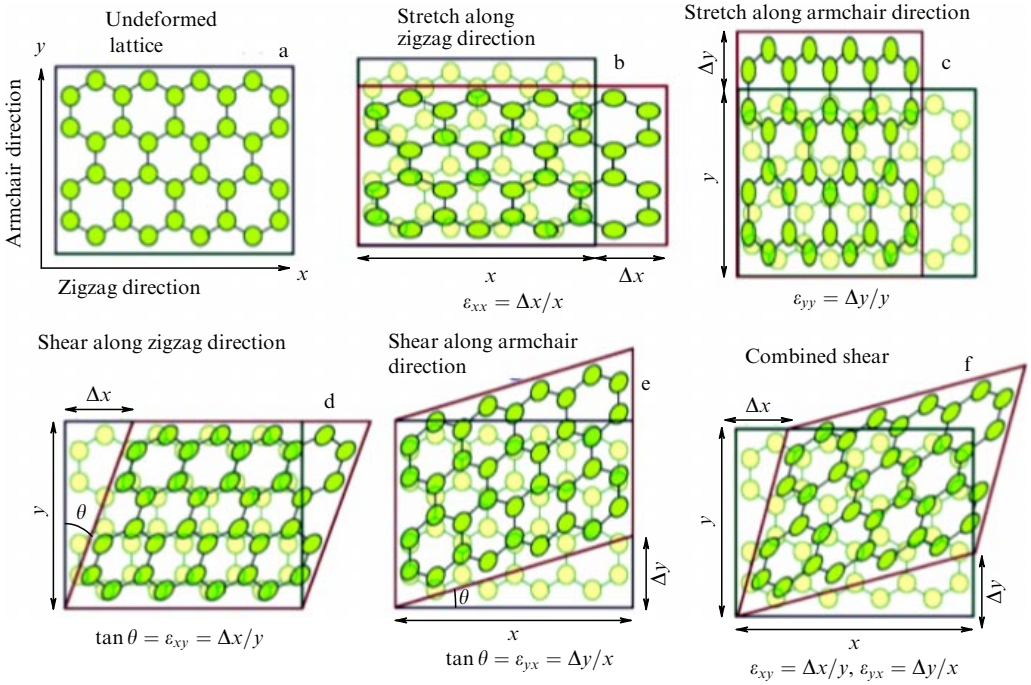

Figure 5. (a) Piece of a graphene lattice subjected to various types of deformations: stretching in (b) zigzag and (c) armchair directions, shearing in (d) zigzag, (e) armchair, and (f) both directions; ε denotes deformation tensor parameters [75].

graphene transferred to SiO_2/Si has a deformation in the range from −0.2 to 0.4, which gradually varies on the scale of several micrometers. As a result of annealing at 100 °C or at a higher temperature, this deformation and the degree of doping of graphene with holes can be varied, which also leads to a change in the position of the Raman modes in the spectra.

3.2 Deformation-induced changes in the band structure of graphene

The absence of a band gap in graphene does not allow controlling the current in transistor structures with a graphene channel: the transistor cannot be shut. Various attempts are being made to open the band gap in graphene; for this, nanoribbons [71], nanoporous graphene [72], and graphene functionalization (for example, the creation of hydrogenated graphene) [73] are used. However, all methods of nanostructuring with the aim of opening the band gap lead to a catastrophic decrease in the mobility of charge carriers, and in some cases also in the conductivity. Methods for creating a band gap in graphene are therefore actively being searched for, with the use of straintronic approaches in particular. Of course, this is not the only possible application of gapped graphene; such a material is of interest, for example, for optoelectronics.

The rupturing deformation of graphene along the armchair direction is 37%, and for deformation along the zigzag direction, the critical value of the change in the bond length is 27% [74]. Figure 5 shows a piece of a graphene lattice subjected to various types of deformations [75].

The prospects for creating a significant energy band gap in the electronic structure of a graphene layer remain a major and highly discussed problem in graphene electronics, because the absence of a band gap limits the possibilities of its application. Review [20] contains the results of theoretical studies of the band gap opening under various deformations of graphene. It is believed that symmetric stretching does not lead to the band gap opening. A mechanically tunable electron energy band gap is possible in two-layer graphene if different uniform deformations are applied to the two layers [76]. It has been shown that the width of the energy band gap can be controlled by adjusting the strength and direction of these deformations.

First-principle (*ab initio*) calculations show that graphene is gapless under uniaxial stretching in the C–C bond plane in accordance with the tight-binding model [77–79]. In the absence of electron–electron interactions, in the framework of linear elasticity theory and the tight-binding approach [80], it was shown that an energy band gap can open in graphene for deformation exceeding a threshold value, and only along preferred directions relative to the base lattice. The threshold deformation, according to different authors, is 16% [81], 20% [82], or 26.7% [83]. The electronic properties of graphene under uniaxial, shear, and combined uniaxial–shear deformations were calculated in [84, 85], where it was shown that combining shear deformations with uniaxial ones allows creating and modulating the band gap in graphene from zero to 0.9 eV under a 17% deformation. Interestingly, the use of a shear component makes the band gap opening possible at a moderate absolute strain, much smaller than the fracture strain of graphene. As shown in Fig. 6, for strain values less than 15% (a) or 11% (b), the density of states (DOS) is linearly dependent on energy near the Fermi level, with a slope that increases as strain increases. The uniaxial and shear strain contributions can be combined in various ways to modulate the band gap. In Fig. 6, we compare the electronic band structures of graphene for various combinations of shear and uniaxial deformation at a fixed value of the strain parameter of $\sim 15\%$.

It was shown in [86] by *ab initio* methods that uniform deformation opens a small band gap only beyond the point of mechanical failure of graphene, contrary to the assertions in the literature based on strong-coupling calculations. It has been found that band gap opening is possible with a sinusoidal nonuniform deformation applied along any direction other than the armchair direction. The largest band gap opens under deformation along the zigzag direction (~ 1.0 eV). The band gap opening has a threshold character with a sharp increase when the ratio of sinusoid amplitude A to deformation period λ exceeds $A/\lambda \sim 0.1$, with the symmetry under inversion preserved. Such deformations can occur in graphene on a boron nitride substrate.

The effect of uniaxial stretching and shear deformations and of their combinations on the possible band gap opening in monolayer graphene (see Fig. 7 and Table 2) was studied in [75]. Deformation-dependent band gap diagrams are plotted over a wide range of deformation tensor parameters (up to 26%, which is close to the predicted fracture point of graphene). It has been established that the use of a combination of shear strain and uniaxial stretching deformations is the simplest way to open and tune the band gap. The results of numerical calculations show that shear deformations can contribute to the band gap opening at the highest elastic deformations, and this is especially efficient for a combination of shear and uniaxial deformations.

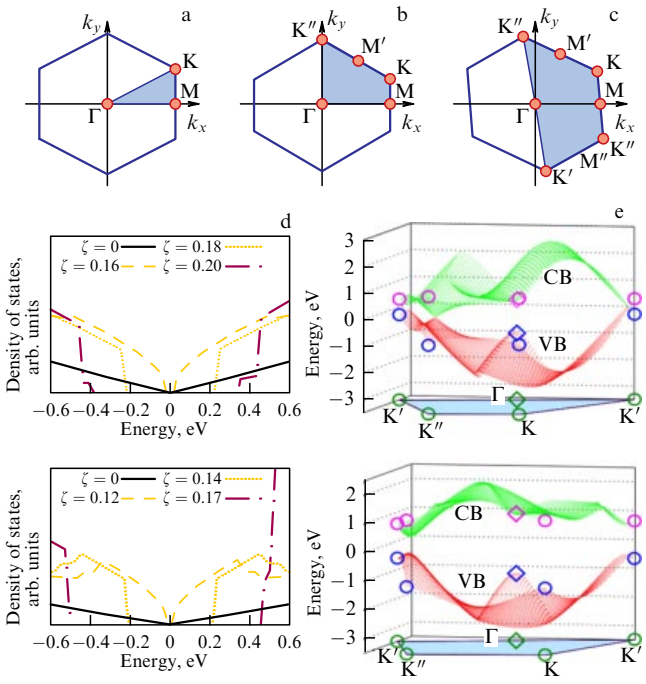

Figure 6. Brillouin zone of graphene under a mechanical load. (a) Undeformed graphene; (b) Brillouin zone under uniaxial deformation with rhombic symmetry; (c) combination of shear deformation with uniaxial deformation. (d) Density of states near the Fermi level as a function of the strain; upper figure: graphene under pure shear strain; lower figure: graphene under joint shear and uniaxial deformation along the armchair direction. Maximum band gap width is observed for the strain parameter equal to 20% and 17%, respectively. (e) Band structures of graphene under various combinations of shear and uniaxial deformation with the deformation parameter fixed at 15%. Upper figure: uniaxial deformation component is applied along the zigzag direction; lower figure: a combination of shear and uniaxial deformation along the armchair direction. CB and VB are conduction and valence bands [86].

A mechanically tunable energy band gap is possible in two-layer graphene if different uniform deformations are applied to the two layers [87]. It has been shown that the width of the energy band gap can be easily controlled by tuning the strength and direction of these deformations.

Thus, tight-binding models and *ab initio* calculations show that uniaxial deformation shifts the Dirac cones away from the K and K′ points below the deformation threshold ($\sim 20\%$) and opens a band gap above this threshold. A similar behavior was also found for shear deformation, but at a lower threshold strain of $\sim 16\%$. Unlike uniaxial and shear deformations, biaxial deformation preserves the crystal symmetry of graphene and hence does not shift the Dirac points and does not open the band gap, but instead changes the slope of the Dirac cones and hence the Fermi velocity [24].

Despite promising theoretical results, experimental studies mostly demonstrate the absence of a band gap, even in the case of strong deformations in graphene. Most graphene films are usually polycrystalline and may in addition contain defects. According to [86], the polycrystalline structure of graphene is a fundamental challenge for the band gap opening, because graphene consists of single-crystal grains that respond to deformation differently due to their different spatial orientations. To obtain the most stable and controlled band gap, graphene samples should be single-crystal ones or consist of single-crystal domains with the same lattice orientation. The presence of a huge number of grain

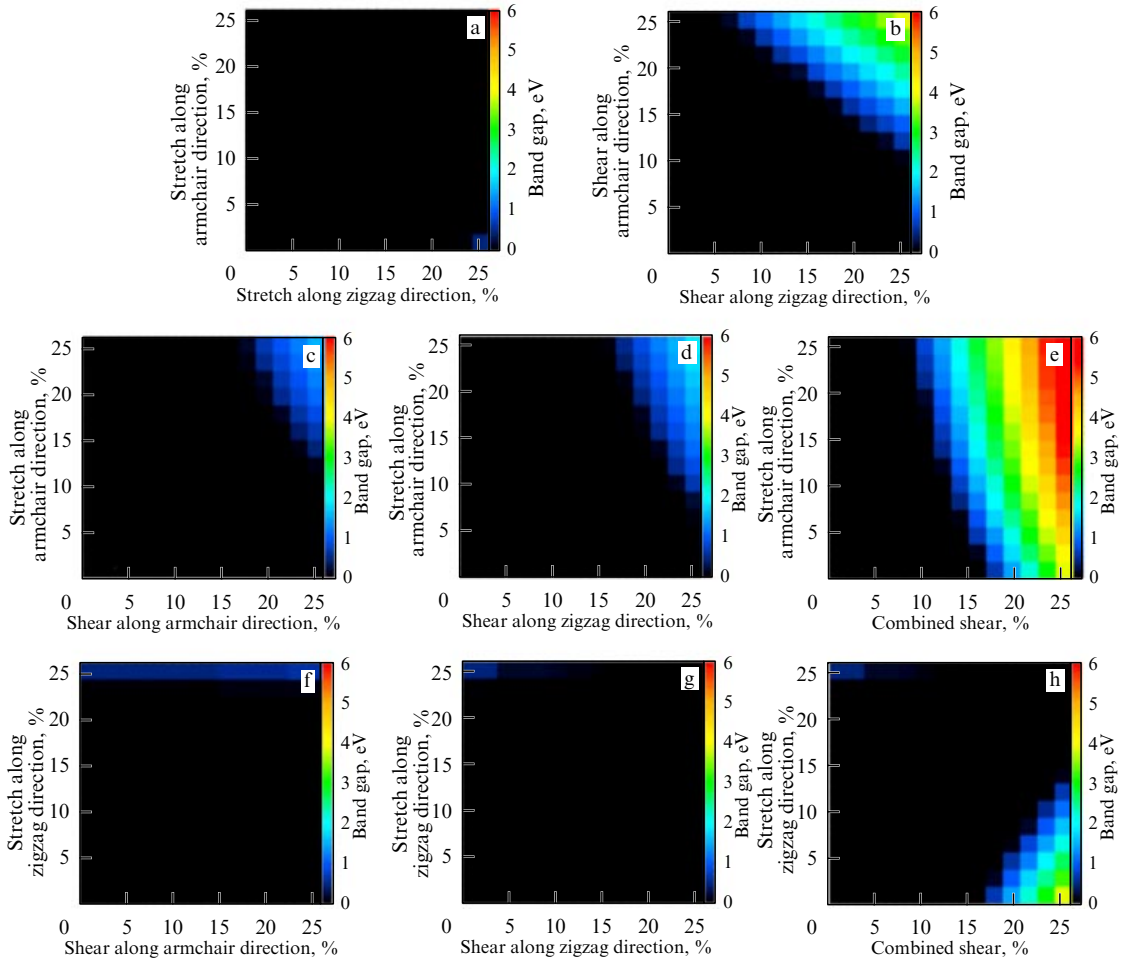

Figure 7. Band gap opening diagrams for graphene under stretching and/or shear deformations (up to 26%): various types of deformation from Fig. 5 [75].

Table 2. Theoretically calculated values for direct band gap E_g in graphene under an ε deformation. ZZ: zigzag direction, AC: armchair direction.

Deformation type	ε, %	E_g, eV	Reference
ZZ stretching	20 – 30	0 – 1.1	[80]
ZZ stretching	26.7 – 40	0 – 2.2	[81]
Shear deformations Combination of uniaxial and shear deformations	20 12	0.60 0.90	[83]
Uniaxial ZZ deformation Uniaxial AC deformation	6.5 18 20	0.6 1.0 0	[88]
Uniaxial deformation Isotropic biaxial deformation Biaxial deformation, ZZ stretching, AC compression Shear deformations	±20 ±20 11(−20AC) ±20	0 0 1.0 0.4	[89]
ZZ stretching	26.5	0.45	[87]
ZZ stretching AC stretching + shear deformations	32 15	0.52 0.58	[90]
ZZ stretching Shear deformations AC stretching + shear deformations AC stretching + AC shear AC stretching + ZZ shear ZZ stretching + AC shear ZZ stretching + shear ZZ ZZ stretching + shear deformation	23 23 23 19 18 24 24 17	0.45 4.0 6.0 1.4 2.0 0.6 0.5 4.0	[75]
Asymmetric stretching of a bilayer	5	0.076	[76]

boundaries in polycrystalline graphene, acting as extended defects, induces electron states near the Dirac point, thereby preventing the band gap opening. This may be one of the reasons why attempts to experimentally observe the energy band gap caused by stretching or shear deformations in polycrystalline graphene samples have been unsuccessful.

In addition, the band gap may not be observed for a number of other reasons. In the case of graphene growth on a faceted SiC surface, the maximum possible band gap in the region of a step, according to theoretical estimates, is 0.20–0.25 eV [91]. Although the stretching deformation of polycrystalline graphene is large (22.5% [92]), this is insufficient for the appearance of a band. Moreover, directional deformation becomes impossible in the case of different grain orientations, and the adsorption of certain impurities on the surface of graphene can strongly affect the band gap opening.

3.3 Conductivity and mobility of charge carriers in graphene under deformation

No less important parameters of graphene for a range of applications are the conductivity and mobility of charge carriers. They are important primarily for the fabrication of transistors and other devices operating at high frequencies. Such structures are expected to operate in the terahertz range, which is not attainable by devices made of other materials. However, a carrier mobility exceeding 10,000–15,000 $cm^2\ V^{-1}\ s^{-1}$ must be ensured to reach that range. The transport properties of transistor structures made of CVD-grown graphene under shear deformations up to 16.7% were studied in [93]. The top gate was made of an ionic liquid, and PDMS (polydimethylsiloxane, highly stretchable dielectric films) was used as a substrate. Shear deformation was applied to the transistor structure thus created. The results obtained are shown in Fig. 8. It can be seen that the position of the neutrality point on the current-voltage curve is virtually unchanged under shear deformations. The conductivity and mobility of carriers increase at relatively small deformations, but then start decreasing significantly (by almost an order of magnitude) at $\varepsilon \sim 5\%$. Such nonmonotonic behavior can be associated with several factors that affect the tested parameters in different ways: the presence of folds, transverse conductive channels, and grain boundaries in graphene.

In another paper by the same authors, CVD graphene was subjected to a stretching deformation of up to 22.5%, created using a piezocrystal [94]. In this case, the transfer characteristics of transistor structures shifted toward higher positive voltages, which corresponds to an increase in the hole concentration in graphene. But the conductivity near the neutrality point, as well as the mobility of electrons and holes, decreased monotonically by about a factor of two as deformation increased.

The decrease in mobility and hence in conductivity observed under relatively low deformations was explained in [93, 94] by two factors: (1) scattering caused by molecular particles contained in the porous structure of the flexible substrate and (2) scattering at domain boundaries in graphene. Despite the high limit deformations, no band gap opening was observed. Thus, deformation cannot be used to create device structures that operate at higher frequencies.

Mechanically stressed ballistic transistors with a graphene channel, as was theoretically shown in [94], can have an on/off current ratio $> 10^4$ under stretching deformation up to $\sim 5\%$. The quantum transistor was modeled on the basis of

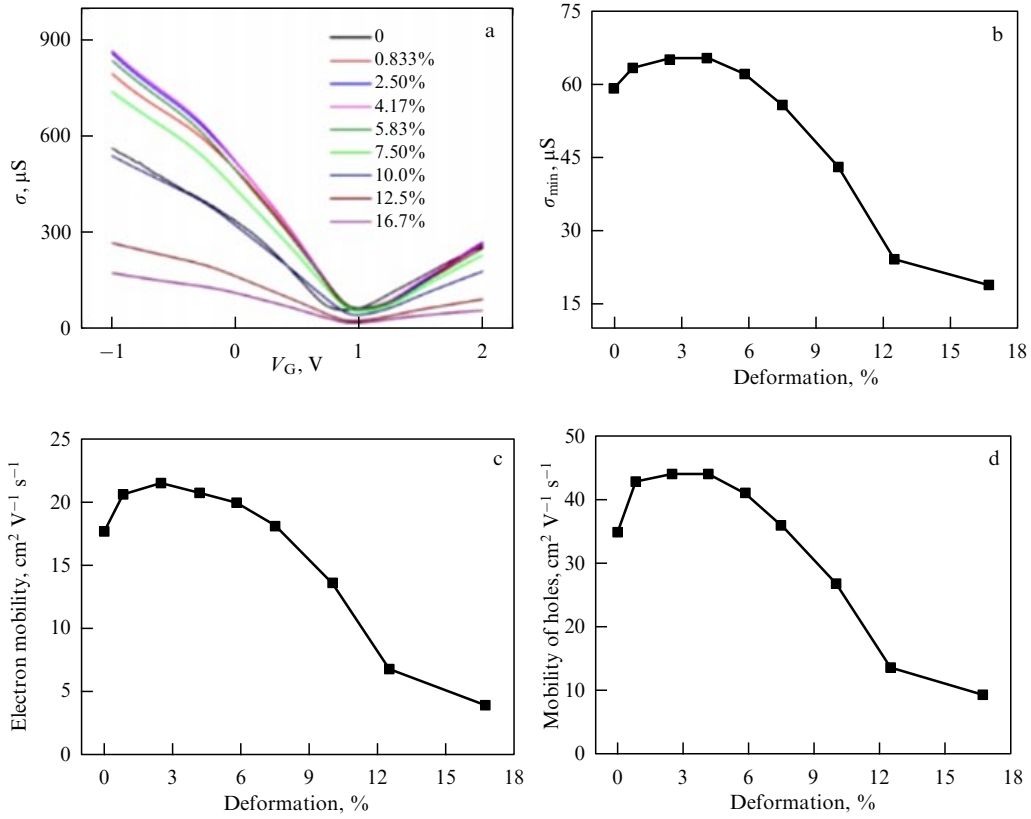

Figure 8. (a) Transfer characteristics of a transistor structure with a graphene channel under various shear deformations. (b) Neutrality point conductivity as a function of deformation. (c) Electron and (d) hole mobility in graphene under various deformations [93].

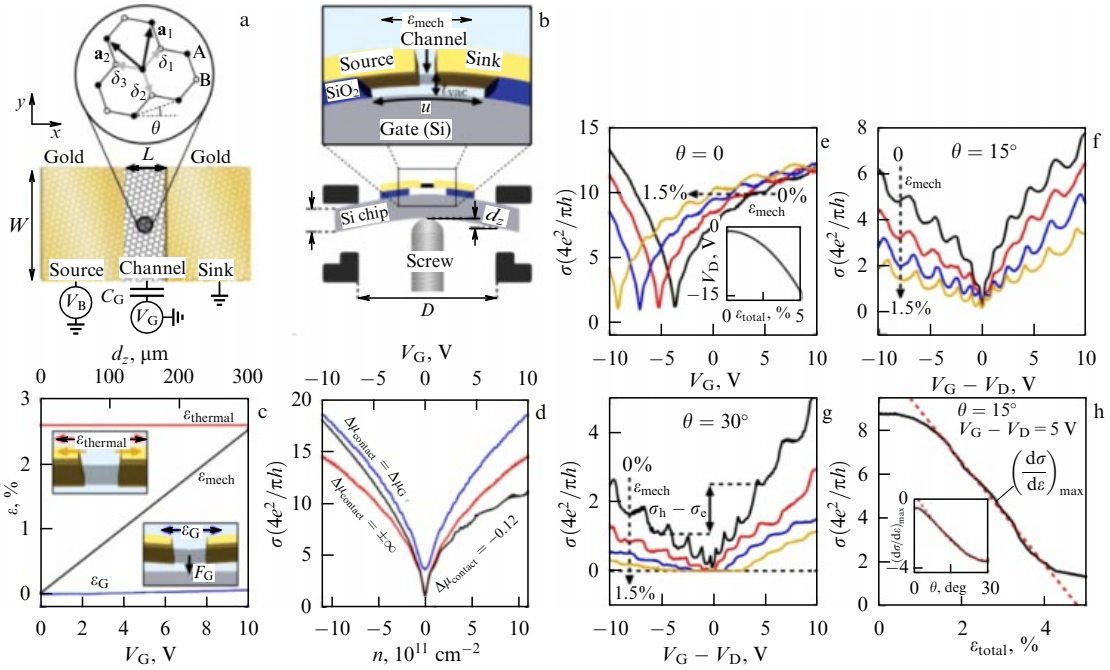

Figure 9. (Color online.) (a) Geometry of a ballistic graphene transistor. Graphene lattice shows crystal orientation θ with respect to the x-axis. (b) Side view of the transistor structure and the device creating deformations. (c) Three sources of deformation in the channel: mechanical motion of the pressure screw (black line), thermal contraction (red) at 1 K, and electrical voltage V_G (blue). Insets: visualization of deformation. (d) Conductivity as a function of the charge density n (lower axis) or V_G (upper axis). Contact doping: $\Delta\mu_{contact} = -0.12$ eV (black), $\pm\infty$ (red), and $\Delta\mu_{contact} = \mu_G$ (blue). (e) Dependence of σ on V_G for $\varepsilon = 0$, 0.5, 1.0, and 1.5 at $\theta = 0$. Deformation shifts the curves. (f) Conductivity at $\theta = 15°$. A rapid decrease in σ with increasing deformation is observed, and resonance peaks are visible. (g) Curves for $\theta = 30°$ show complete suppression of σ under deformation. (h) Conductivity as a function of total deformation at $\theta = 15°$ and slope dependence on angle θ [94].

suspended graphene. In Fig. 9, we show schematic images of the transistor and the obtained characteristics for different orientations (θ angles) between the zigzag direction and the x-axis directed along the transistor channel. The engineering of quantum transport in 2D materials by deformation is currently an important area of straintronics. The authors propose a theoretical platform for the engineering of ballistic charge transfer in graphene using uniaxial deformation. In particular, the use of deformations solves an important problem with transistors with a graphene channel: controlling the current in the channel, at least at low temperatures.

Ab initio calculations have shown that a combination of electron or hole doping with biaxial tensile deformation can transform graphene into a superconductor [95]. The authors found that, at experimentally available doping levels (4×10^{14} cm^{-2}) and deformations (16%), the critical superconductivity temperature T_c must reach 30 K, which is relatively high. For comparison, a graphene monolayer grown directly on a thin Ru (0001) superconducting film exhibits a superconducting state at temperatures below 2.1 K [96]. Superconductivity induced by doping graphene was discovered in [97]. Adsorption of a layer of Li atoms on a graphene monolayer gives rise to a stable superconducting state at temperatures below 5.9 K. The authors of [98] also showed that graphene modified with calcium becomes superconducting at a temperature of about 6 K. It is therefore quite reasonable to expect that superconducting graphene with a high T_c can be realized experimentally via a combination of doping and deformation. Superconductors are used in quantum interferometers, supersensitive magnetometers, photon detectors, and medicine to obtain magnetograms of various organs, etc. Further study of the properties of superconductors, their fabrication methods, and the optimization of parameters will also enhance their applications.

Under a strong local distortion of a graphene lattice, electrons in the deformed region start moving along closed trajectories, as if they were placed in an external magnetic field, as was predicted theoretically in [99, 100] (Fig. 10). Such a 'magnetic field' is called pseudomagnetic; the greater the lattice deformation attained, the stronger this magnetic field. A nonuniform distribution of deformations can generate a strong pseudomagnetic field and hence lead to the observation of Landau levels (the energy levels of a charged particle in a magnetic field) and the quantum Hall effect. This effect was experimentally observed in the study of graphene nanoblisters using a scanning tunneling spectroscopy probe [101]. As a result, peaks were observed in the current-voltage characteristics measured in the blister region. Scanning tunneling spectroscopy has shown the presence of Landau levels in the region of nanoblisters with very high energies corresponding to a magnetic field of about 350 T. When graphene was eventually doped, its characteristics changed from semimetallic to semiconducting if the Fermi level was located between the Landau levels. We note that, due to the linear dispersion in graphene, the Landau levels are not equidistant, and there is no peak in the DOS near the Dirac point (Fig. 10g, h). A study of the effect of deformation on the spectra of Landau levels in graphene within the density functional theory (DFT) showed in [102] that uniaxial deformation induces compression of the spectra of Landau levels for both crystallographic directions (armchair and zigzag) of the applied deformation. It turns out that, to study the effect of extreme magnetic fields on the electrical

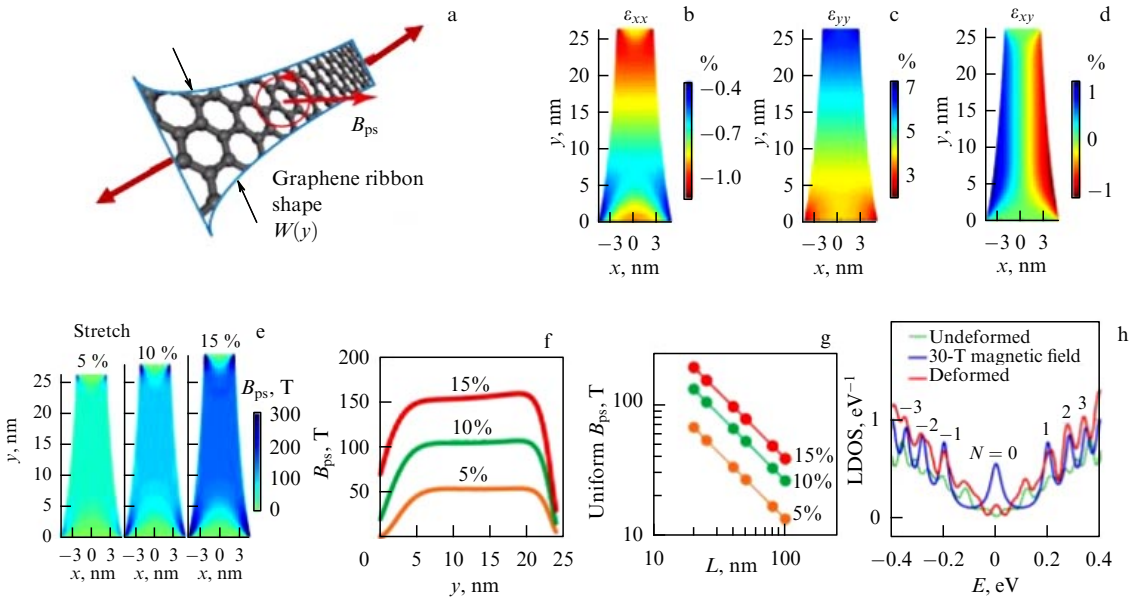

Figure 10. (Color online.) Generation of uniform pseudomagnetic fields in a flat graphene ribbon under uniaxial stretching [102]. (a) Graphene nanoribbon under uniaxial stretching that produces a pseudomagnetic field B_{ps}. Red circle shows cyclotron orbits of carriers in the field that leads to the appearance of Landau levels (shown in Figs g and h). (b–d) Resultant components of deformation in graphene under uniaxial 5% stretching. (e) Resultant pseudomagnetic fields in the graphene nanoribbon shown in Fig. a, at the respective uniaxial deformations of 5%, 10%, and 15%. (f) Pseudomagnetic field strength as a function of position along the central line of the graphene ribbon for various deformations. (g) Diagram of a low-energy dispersion of graphene with quantized Landau levels in a magnetic field [100]. (h) Local density of states (LDOS) of undeformed graphene, graphene in a magnetic field, and deformed graphene. The LDOS fluctuations in the undeformed case and the magnetic field are a result of the finite size of the cell.

properties of solids, magnetic fields are not needed: they can be replaced by deformation.

An alternative method for achieving pseudomagnetic fields with their uniform distribution over large areas by stretching a nanoribbon along one axis was proposed in [102]. The authors found the shape of a graphene ribbon such that stretching at its ends gives rise to a uniform pseudomagnetic field: with a linear decrease in the width of the graphene domain in the lateral graphene/graphane and graphene/h-BN heterostructures due to the broadening of a part of the graphane or h-BN ribbon, different narrowing scales result in different field strengths.

Thus, the use of deformation to engineer the electronic structure of graphene at the nanoscale not only is interesting from the fundamental standpoint but also can be very useful for practical purposes. For example, if conditions for the ballistic mode of carrier transport are ensured during deformation, it becomes possible to control the current in the transistor channel. The possibility of observing superconductivity at a relatively high temperature, which is quite interesting for applications, is also predicted theoretically.

3.4 Functionalized graphene under deformation

The functionalization of graphene, as shown in a huge number of studies, can lead to the band gap opening in graphene. *Ab initio* calculations were used to study the electronic properties of fully hydrogenated bigraphene as a function of biaxial deformation [103]. After complete hydrogenation, bilayer graphene was found to exhibit semiconducting characteristics with a wide direct band gap. We can see from Fig. 11 that the band gap can be continuously controlled by biaxial deformation. Compression can induce a semiconductor-to-metal transition for hydrogenated bigraphene at a 13% stretching deformation. An analysis of the DOS showed

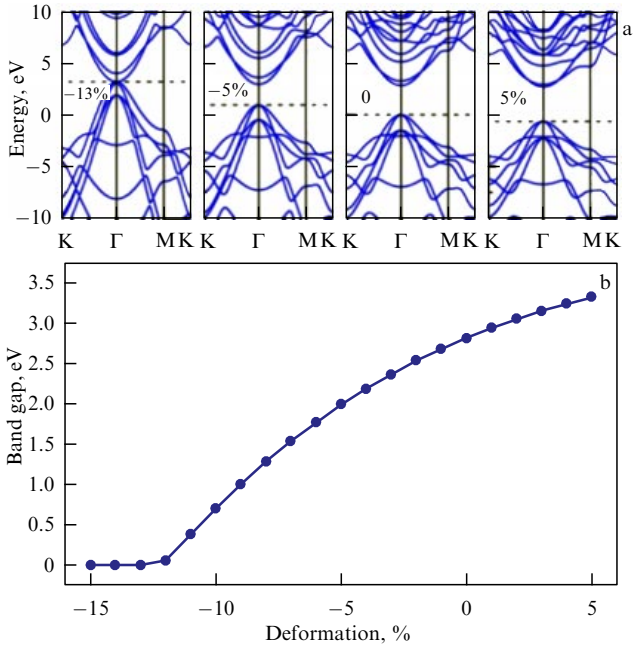

Figure 11. (a) Band structures of hydrogenated bigraphene corresponding to different biaxial deformations. Zero-energy point is chosen equal to the energy of the undeformed bilayer. (b) Band gap width of hydrogenated bigraphene as a function of biaxial deformation [103].

that the position of the conduction band minimum is determined by the antibound states of the p_z orbitals of hydrogenated carbon atoms and the s-electrons of hydrogen atoms, which are not significantly affected by biaxial deformation. On the other hand, the bonds of the p_x and p_y orbitals of carbon atoms, which determine the position of the

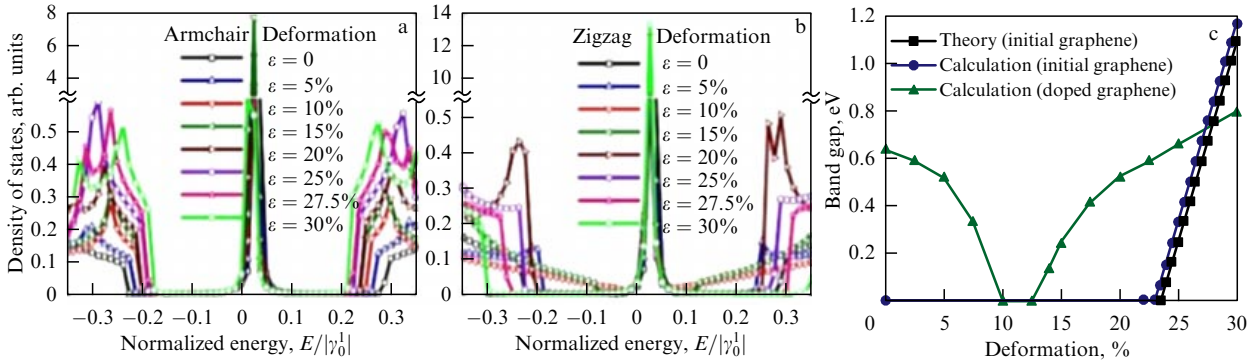

Figure 12. (Color online.) (a, b) DOS for a graphene monolayer with 3.125% of ordered resonant impurities (O- or H-containing molecules) for various tensile stresses up to 30% along the (a) armchair and (b) zigzag directions. (c) Comparison of the analytically [76] and numerically [79] calculated band gap energies under uniaxial deformation along the zigzag direction for monolayer graphene without defects (squares and dots) and with 3.125% of ordered hydroxyl groups (triangles) [106].

valence band maximum, change sharply under biaxial deformation (they are enhanced by stretching deformation and weakened by compressive deformation). This immediately leads to a shift in the position of the valence band maximum. The ability to tune the band gap of hydrogenated bigraphene by mechanical deformation provides a way to create electromechanical devices based on two-layer graphene.

Ab initio calculations were used in [104] to theoretically study the electronic properties of 2D crystalline graphene oxide (GO) with the carbon/oxygen ratio of 1:1. It was found that the GO band gap is sensitive to changes in lattice angles due to bonds with oxygen groups. Initially, for a hexagonal system without distortions, the angle is 120°; when varying it in the range of 120°–134°, the band gap changes from 0 to more than 1.3 eV, and, as the lattice angle increases, the band gap becomes an indirect one. This fact determines the strong dependence of the GO properties on external mechanical stresses.

The strong effect of the adsorption of O- or H-containing molecules on the electron states and charge transfer or localization in graphene with various configurations of point defects was shown in [105]. Resonant impurities (O- or H-containing molecules) and vacancies equally change the DOS of deformed graphene: as calculations show, they lead to an increase in the central peak near the Dirac point (Fig. 12) [106]. The fundamental difference between O- or H-containing molecules and vacancies with regard to their effect on the spectrum of states is the position of the central peak (impurities/vacancies), which is centered at the neutrality point in the case of vacancies and is shifted from this position for hydroxyl groups due to the nonzero (positive) potential of molecules. Figure 12 shows DOS values around the Fermi level as a function of stretching deformation (30%) for single-layer graphene with a fixed concentration of ordered H or O adatoms. The band gap monotonically decreases as the deformation increases in the armchair direction. But, in the case of deformation in the zigzag direction, the band gap decreases until it completely disappears at 10%, and then, at a deformation threshold value of 12.5%, the band gap reappears and increases as the deformation increases. It is important that this threshold value be lower than those previously estimated for perfect defect-free graphene layers subjected to uniaxial zigzag (23% [76]) or shear deformation (16% [79]), and practically coincides with the expected value that combines shear and uniaxial deformations in the armchair direction (12% [79]).

As another example of the use of deformations to control the properties of materials, the band gap of nanoribbons formed by chemical functionalization of graphene ribbons can vary by up to 30% due to mechanical stresses directed across the nanoribbons [107].

In general, a significant change in the band structure at relatively low deformations is predicted theoretically for functionalized graphene, which is interesting from the practical standpoint. The predominance of theoretical studies must also be noted.

4. Straintronics of transition-metal dichalcogenides

Among 2D materials, single-layer molybdenum disulfide MoS_2 has recently attracted considerable attention. It belongs to the transition-metal dichalcogenides and has a high potential for use in field-effect transistors (FETs) [108], phototransistors [109], flexible optoelectronic and logic devices [110, 111], and lithium-ion batteries [112]. Unlike monatomic graphene, MoS_2 is a structure with three atomic sublayers: a transition-metal (Mo) atomic layer is located between two layers of sulfur atoms. This allows MoS_2 to exist in different polymorphic phases and therefore to demonstrate varying physical and chemical properties [113]. Rupture deformations for MoS_2 are low, $\sim 11\%$. The most common are the octahedral (1T) phase and the phase with trigonal prismatic geometry (2H) [114]. The 2H MoS_2 phase has semiconducting properties with a direct band gap [115]. The 1T phase is metallic and metastable compared to the 2H phase [116].

A structural transition is known to occur in single-layer MoS_2 under stretching deformation. It is associated with a relative shift of the two outer S-atomic layers and leads to a semiconductor–metal phase transition [117, 118]. This transition is observed under a stretching deformation of $\sim 19\%$ [118]. Under strong uniaxial compression, one more phase transition occurs along the armchair direction [119]. The new phase was found to be stable and also metallically conductive.

Let us consider changes in the band structure of transition-metal dichalcogenides under deformation. It is known that, with a decrease in the number of layers of MoS_2 and other transition-metal dichalcogenides, the transition from an indirect-gap semiconductor to a direct-gap semiconductor occurs with a simultaneous gradual increase in the band gap (from 1.2 to 1.8 eV for monolayer MoS_2) [120, 121].

The rates of decrease in the band gap under stretching were determined in [122] in experiments on nanoindentation of MoS_2 membranes with a thickness of 1 to 3 monolayers. The study of the piezoresistive behavior allowed determining the relative tensile sensitivity coefficient of these films. The authors observed a decrease in the band gap under deformation at the respective rates of -77.3 ± 10, -116.7 ± 10, and -22.7 ± 6 meV/% for single-layer, two-layer, and three-layer MoS_2. The stronger effect for two-layer MoS_2 is related to a decrease in the distance between the layers, which affects the orbital hybridization between the planes. In the case of three layers, the band gap becomes indirect and decreases at a different rate. The results obtained are in excellent agreement with theoretical predictions [123, 124]. Optical measurements for a monolayer MoS_2 in the case of stretching deformation caused by bending also showed that the rate of decrease in the direct band gap is 70 meV/% [125]. Similar experiments on the study of photoluminescence (PL) of curved structures [126] gave another value for the rate of change in the band gap of monolayer MoS_2: -27 ± 2 meV/% for deformations up to 1.1%. We especially note that the change in the band gap is reversible and is reproduced under cyclic deformations.

The change in the band gap of MoS_2 films of various thicknesses depending on uniaxial and biaxial deformations was studied in [127, 128]. In the case of uniaxial deformation, the optical width of the direct band gap decreases almost linearly at a rate of -45 meV/% for an MoS_2 monolayer and -120 meV/% for a two-layer MoS_2. In the case of biaxial deformation of a structure consisting of graphene on three-layer MoS_2, the opposite effect is observed, and the rate of change in the optical band gap is then much higher, ~ 300 meV/%.

For an MoS_2 CVD film on suspension membranes under biaxial deformation caused by gas pressure, the authors of [129] obtained a higher optical band gap change rate, 99 meV/%. The biaxial deformation occurring at the center of the device can be estimated as $\varepsilon = \sigma(v)(\delta/a)^2$, where a is the radius of the hole under the membrane, δ is the height of the membrane dome above the hole, and $\sigma(v)$ is a parameter that depends only on Poisson's ratio v. For MoS_2, $v = 0.29$, and the result is $\sigma = 0.709$. The results of studies on the effect of deformation on the energy and intensity of peaks in the PL spectrum and on the positions and shift rates of two Raman modes in MoS_2 layers are shown in Fig. 13. The Raman spectrum modes shift linearly at a rate of -1.7 cm^{-1}/% for A_{1g} and -5.2 cm^{-1}/% for E^1_{2g}, which agrees well with theoretical predictions [130] and previous experiments [131].

A tunable optoelectronic material with a spatially variable band gap is promising for use in photovoltaics, photocatalysis, and photodetection. Elastic deformation can potentially be used to achieve fast, local, and reversible band gap tuning and the creation of artificial atoms in MoS_2 films [123]. The geometry of a 'funnel' surrounded by semiconducting buffers can lead to selective accumulation of carriers in desired regions (Fig. 14). The operation of the proposed device requires that the relaxation of inelastic deformation due to the appearance of a dislocation or destruction be avoided [132]. The stress gradient and hence the elastic deformation gradient are maintained by a concentrated load arranged such that stress is inversely proportional to the bend radius. Such a deformation field resembles the potential field of a 2D

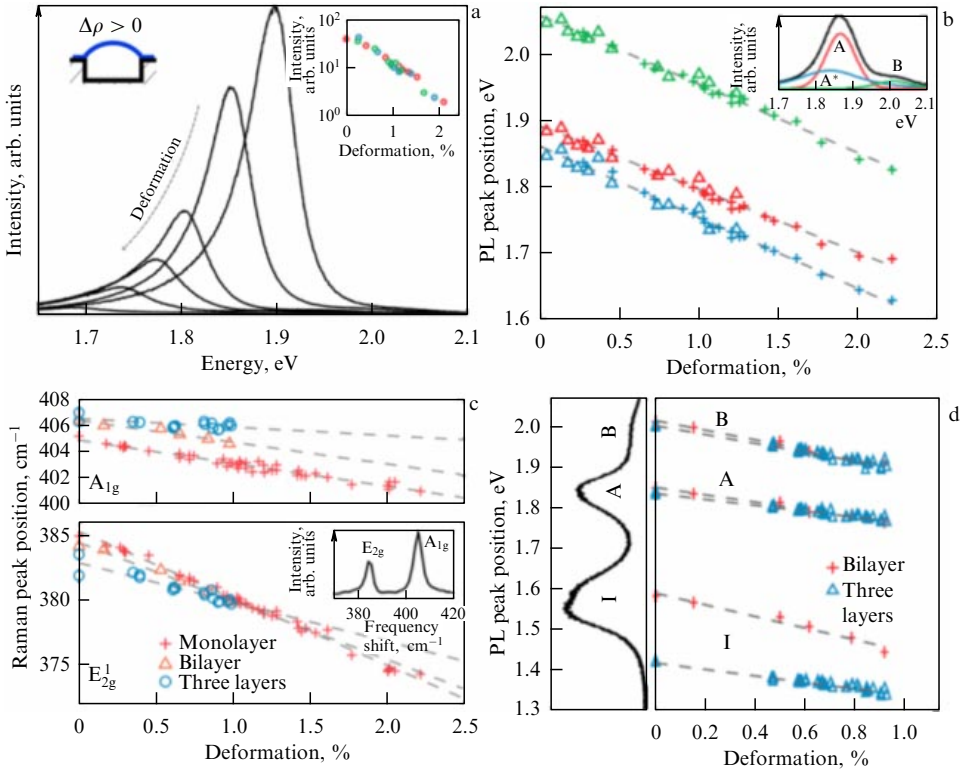

Figure 13. (Color online.) (a) PL spectra of an MoS_2 monolayer under various biaxial deformations, and the relation between deformation and the magnitude of the A peak (inset). Magnitudes are normalized to Raman peak A_{1g}. (b) Position of the exciton peaks A (red), A^- (blue), and B (green) as a function of biaxial deformation for devices to test for coronary vascular diseases (crosses) and for layered monolayers (triangles) obtained by exfoliation. (c) Positions of the E^1_{2g} and A_{1g} peaks in the Raman spectra as a function of biaxial deformation for membranes of various thicknesses. (d) PL spectrum of a two-layer film and positions of the A, B, and I peaks depending on the biaxial deformation of films of different thicknesses [129].

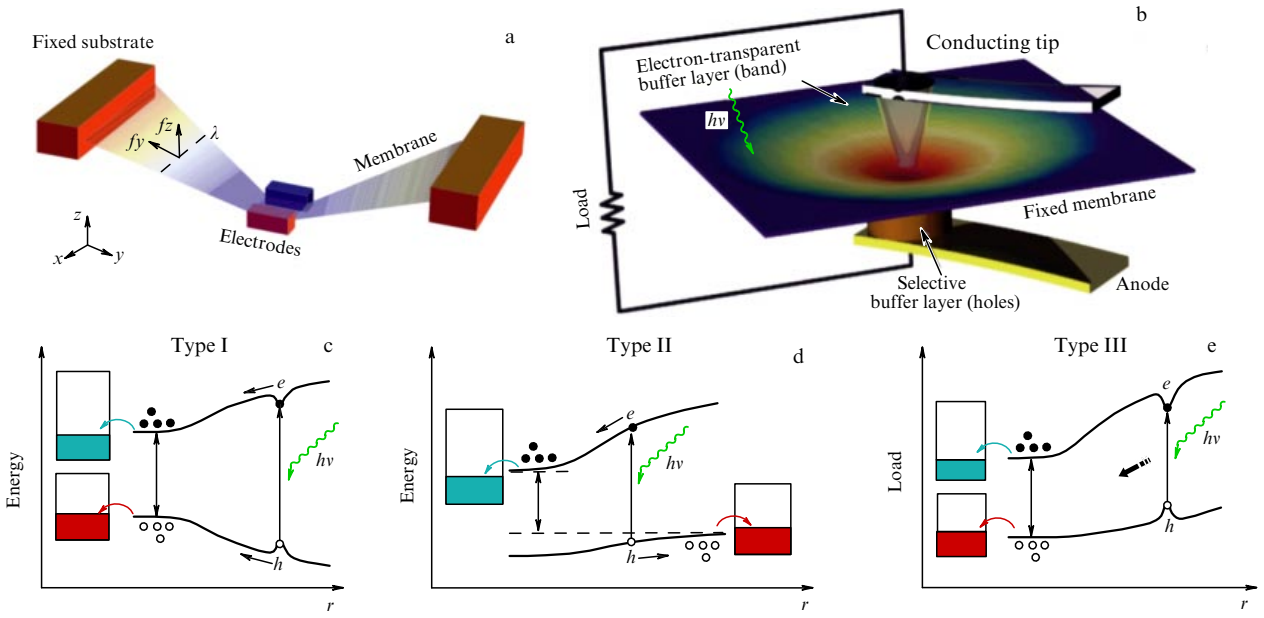

Figure 14. Introduction of nonuniform deformations into MoS_2 layers. (a) Diagram of nonuniformly deformed membrane ribbons of various widths. Two electrodes mechanically impose a vertical displacement on the central region of the membrane. (b) Diagram of the device for applying elastic deformation to create an artificial atom. Although most of the electrodes are metallic, they are coated with semiconducting buffers to facilitate the selective collection of quasiparticles. This device completely removes the edges of the membrane ribbon, which may otherwise be the preferred locations for defects to occur. (c–e) Three broadband carrier collection mechanisms arising from different ribbon bending profiles and exciton binding in a semiconducting membrane due to mechanical stresses [123].

hydrogen atom, but on a much larger spatial scale. It is in this sense that a mechanically deformed atomic membrane can be regarded as a mesoscopic 'artificial atom,' with the electronic and optical properties strongly dependent on deformation fields.

The modification of the band structure under stretching deformation was also studied for mechanically detached WS_2 and MoS_2 monolayers (with the respective band gaps of 2.03 and 1.87 eV) on a flexible substrate using microphotoluminescence spectroscopy at room temperature [133]. Under deformation, the peaks demonstrated redshifts, indicating a decrease in the band gaps. Under stress, the band gap decreases linearly and is the same for deformation along the armchair and zigzag directions. For a 1% deformation, the observed decrease in the band gap is 64 meV for WS_2 and 55 meV for MoS_2. The use of PL and Raman spectroscopy to study the evolution of the electronic band structure of CVD-grown WS_2 under uniaxial stretching deformation also showed that the transition from a direct to an indirect band gap occurs at a strain of 2.5% [134]. The ability to change the band structure of a material by deformation is promising for its use in flexible electronics and optoelectronics.

The effect of biaxial stretching and compressive deformations on the electronic properties of a WSe_2 monolayer was considered within DFT calculations in [135]. Under biaxial stretching, the WSe_2 monolayer preserves a direct band gap, with a continuous decrease in its width (eventually, with a transition to a metal) at a strain exceeding 13%. Under biaxial compression, a transition to an indirect band gap occurs, the band gap width decreases with increasing strain, and the material becomes a metal at a strain of $\sim 7\%$. It is shown that stretching deformation is more efficient than compressive deformation as regards decreasing the band gap. Biaxial stretching changes the relative position of atoms and the length of bonds, and π bonds are apparently formed between W and Se, characterized by a high sensitivity to deformation. An experimental comparison of the optical properties of four monolayers of transition-metal dichalcogenides (MoS_2, $MoSe_2$, WS_2, and WSe_2) using biaxial deformation was carried out in [136]. For stretching deformation, a redshift of the band gap was found, which reaches a value of 95 meV/% for WS_2 deposited on polypropylene. Changes in the band gap depending on the stretching or compression of the substrate for different materials are related as $MoSe_2 < MoS_2 < WSe_2 < WS_2$.

First-principle calculations of the structural, electronic, and vibrational properties of WS_2, WSe_2, and WTe_2 monolayers were performed in [137] with the strong spin–orbit coupling taken into account. The transition from a direct to an indirect band gap was achieved at compression strains of 1% (WS_2), 1.5% (WSe_2), and 2% (WTe_2). The band gap passes through a maximum under compressive deformation and decreases monotonically under stretching deformation. In all three compounds, a strong spin splitting of the valence band was found, additionally enhanced by stretching.

The effect of stretching deformation (up to 8%) on the electronic structure of 2D trichalcogenide transition metals (MX_3 monolayers with M = Ti, Zr, Hf, Nb and X = S, Se, Te) was studied by DFT calculations in [138]. Undeformed TiS_3, ZrS_3, $ZrSe_3$, HfS_3, $HfSe_3$, and NbS_3 monolayers are semiconductors with a band gap ranging from 0.80 to 1.94 eV. DFT calculations show that biaxial and uniaxial stretching deformations can effectively modify the band gap of many monolayers in this class of materials. In particular, it was found that ZrS_3 and HfS_3 monolayers undergo a transition from an indirect to a direct band gap with increasing stretching deformation. The value of the indirect band gap in $ZrSe_3$ and $HfSe_3$ monolayers increases upon increasing the

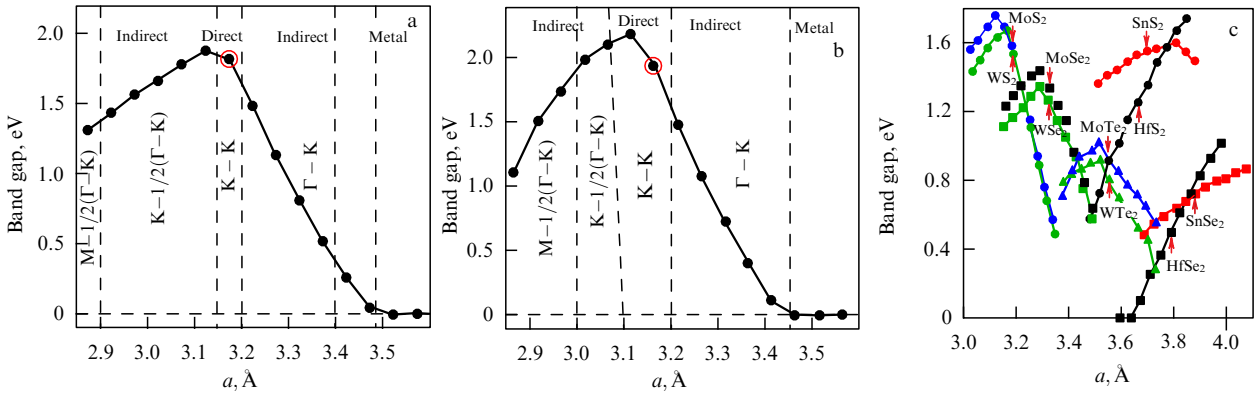

Figure 15. Band gap evolution of (a) MoS_2 and (b) WS_2 monolayers under isotropic stretching and compression. K points at which the top of the valence band and the bottom of the conduction band are located are indicated. Equilibrium structures are marked with red circles [139]. (c) Theoretical band gap width for various MX_2 monolayers as a function of the lattice constant modified by uniform isotropic deformation ranges from −5% to 5%. Red arrows indicate the equilibrium lattice constant for each monolayer [140].

stretching deformation. The respective $ZrTe_3$ and $HfTe_3$ monolayers were shown to be metals that allow conversion into indirect-gap semiconductors at $\varepsilon = 4\%$ and 6%. The TiS_3 monolayer can maintain a direct band gap for biaxial or uniaxial stretching deformations up to 8%. Variation of the direct band gap in MS_3 (with M = Hf, Ti, or Zr) under deformation and the transition from metallic to semiconducting properties of MTe_3 (with M = Hf or Zr) demonstrate interesting possibilities for producing artificial layered structures with size-controlled direct/indirect band gaps for applications in optoelectronics and flexible electronic devices.

In Fig. 15a, b, we show the evolution of the band gap for MoS_2 and WS_2 hexagonal monolayers under isotropic 2D deformation [139]. In equilibrium, single layers have a direct band gap at the K point. Under stretching deformation, the band gap decreases linearly and becomes indirect in passing from the Γ to the K point. Eventually, at a stretching of about 11%, the band gap disappears, and the monolayers acquire metallic conductivity. Under this stretching, the bonds are stretched, but not yet broken. A similar but weaker dependence is also observed when a compressive deformation is applied to the monolayer. Uniaxial stretching deformation leads to a similar decrease in the band gap with a possible transition to the metallic state. In this case, however, the changes at specific values of stretching or compression are smaller than those under isotropic 2D deformations. Similar data were obtained in [140] for a number of materials and are presented in Fig. 15c. These results are in very good agreement with the results in [141–143].

A comparison of the results of experiments on deformation in the atomically thin 2D semiconductors MoS_2, WSe_2, and $ReSe_2$, together with some theoretical predictions for the band gap change, are presented in review [36]. In Fig. 16, we summarize the maximum band gap changes measured by optical spectroscopy methods for the maximum attainable deformations. Some theoretical predictions for the change in the band gap under large deformations are also included in Fig. 16 to illustrate the prospects for possible modification of the band structure in atomically thin semiconducting materials at the maximum deformation they can withstand before rupture.

Tuning the band gap of a semiconductor by deformation is an interesting chance to control the electrical and

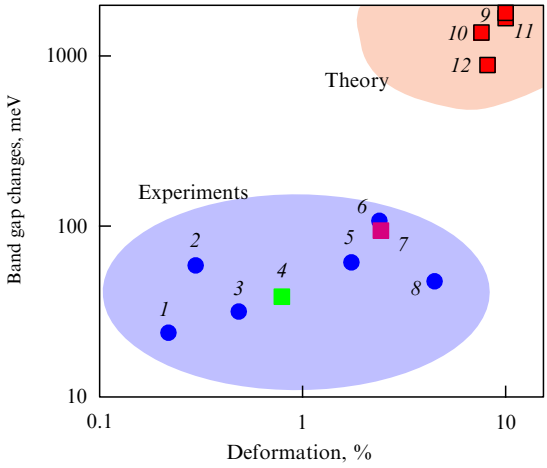

Figure 16. (Color online.) Experimental and theoretical data on the effect of deformations on the band gap width in atomically thin MoS_2 layers (blue dots *1–3*, *5*, *6*, *8*), WSe_2 (green square *4*), and $ReSe_2$ (purple square *7*). Theoretical predictions of the change in the band gap width in single-layer MoS_2 at the maximum possible deformations are also shown. For comparison [36]: *1* — [146], *2* — [137], *3* — [123], *4*, *9* — [144], *5* — [148], *6* — [136], *7* — [124], *8* — [130], *10*, *12* — [145], *11* — [147].

optical properties of 2D materials. As was shown in [149], controlling the level of deformation allows changing the photosensitivity of a detector made of MoS_2 by 2 to 3 orders of magnitude, the response time from 80 ms to 1.5 s, and the spectral bandwidth with a coefficient of 135 meV/% or 58 nm/%. The rapid tuning of such photodetectors opens the possibility of fabricating an artificial device that mimics the functions of the human eye. Therefore, 2D transition-metal dichalcogenides hold great promise for future straintronic devices (as tunable photonic cells), where deformation is used as a regulator to adapt their properties. MoS_2 photodetectors can be tuned from a state with a narrow bandwidth and low sensitivity and to a broadband, high-sensitivity state.

5. Silicene, germanene, phosphorene, and other graphene-like monolayer materials

Silicene and germanene are 2D allotropic modifications of silicon and germanium with a 2D crystal structure similar to that of graphene. Silicene and germanene are zero-gap

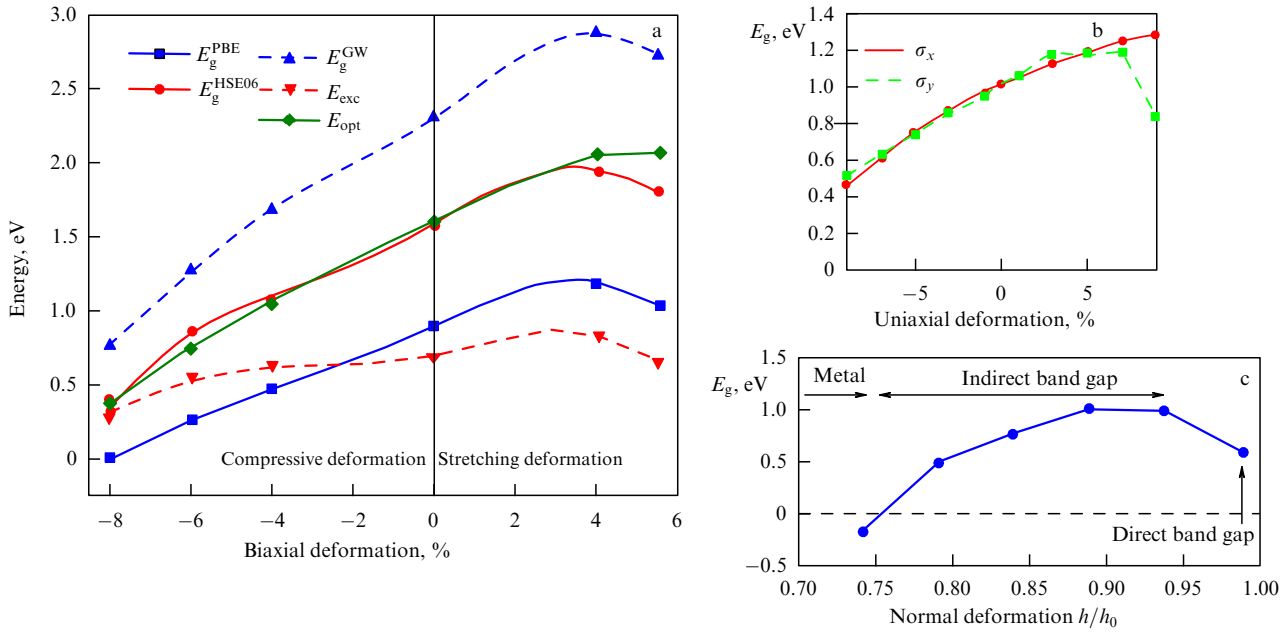

Figure 17. Uniform deformation of a black phosphorus monolayer. (a) Evolution of the electron band gap (E_g, calculated by different methods) and the optical band gap (E_{opt}) of single-layer black phosphorus under biaxial deformation. Dependence of exciton binding energy E_{exc} on strain is also shown. The various numerical methods used are indicated by superscripts [154]. (b) Evolution of the band gap under uniaxial deformation [155]. (c) Band gap vs. normal compressive deformation; $2h_0$ is the initial thickness of the black phosphorus monolayer [156].

semimetals with a linear Dirac cone near the Fermi energy. Similarly, phosphorene is a 2D modification of black phosphorus, obtained by slicing black phosphorus into monatomic layers, and is a semiconductor with a direct band gap of 1.75 eV. The band structures of these materials are also affected by uniform deformation [150–152]. Research results show that the width of the band gap at the Dirac points for silicene increases under compressive deformations at the level of several millielectronvolts. Germanene has an energy band gap of ~ 24 meV under similar conditions. The characteristic bent structure of silicene and germanene leads to a deformation-induced self-doping phenomenon, as shown in first-principle calculations [153]. The Dirac point was found to move below the Fermi level for compressive deformations, resulting in n-doped samples, while p-type doping can be achieved under stretching. In [152], direct band gaps of 264, 335, and 238 meV at the K point were found under 4% uniaxial compression, biaxial compression, and asymmetric deformation. When stretching deformation is applied, the band gap width is approximately three times smaller. With a further increase in stress above 8%, silicene turns into a metal for both types of deformation. The maximum tensile strength is estimated as 3.4 GPa.

The effect of voltage on the electronic and mechanical properties of single-layer black phosphorus was studied with first-principle calculations in [154, 156, 157]. A detailed comparison of the electron band structures of black phosphorus obtained with various numerical methods is presented in [154]. It turns out that the electronic and optical band gaps and the binding energy of excitons increase (decrease) under stretching (compressive) deformation [154, 157]. For biaxial deformation, this trend is shown in Fig. 17a. The applied stretching deformation significantly enhances the transport of electrons along the black phosphorus zigzag direction. Uniaxial deformation gives similar results (Fig. 17b) with a transition from a straight to an indirect band gap at a compressive deformation of the order of 5% [155]. Deformation perpendicular to the black phosphorus layer was studied in [156]. This type of deformation leads primarily to a direct–indirect band gap transition, and a semiconductor-to-metal transition is expected under stronger uniaxial deformations, of the order of 24 GPa. The measured value of the optical band gap width for single-layer black phosphorus is about 1.45 eV [155], which is in good agreement with the value of 1.61 eV calculated in [154].

The use of deformations as an engineering method for graphene-like monolayer materials leads to significant changes in the band structure and results in doping the materials and hence in a change in transport properties. Prospects for controlling the band structure and electrophysical properties have been mainly outlined in theoretical studies. Experimental data for these materials are currently scarce. Experimental work on black phosphorus monolayers, promising for the creation of new photovoltaic devices that cover a wide range of the solar spectrum, is limited by the low stability of this material due to its oxidation in air.

6. Deformation engineering of 2D materials

Device structures using 2D materials are actively being developed for flexible electronics, and deformation engineering is widely used as an important factor to control the properties of raw materials and device structures. The goal of this approach is to use mechanical stresses to tune the electronic and photonic characteristics of 2D materials and ultimately to create promising devices based on them. Recent experiments on the deformation engineering of 2D materials have shown both new possibilities for fundamental physics and unexpected applications of straintronics approaches. We consider some recent advances in applying mechanical deformations to vary the properties of 2D materials for their use in nanoelectronics.

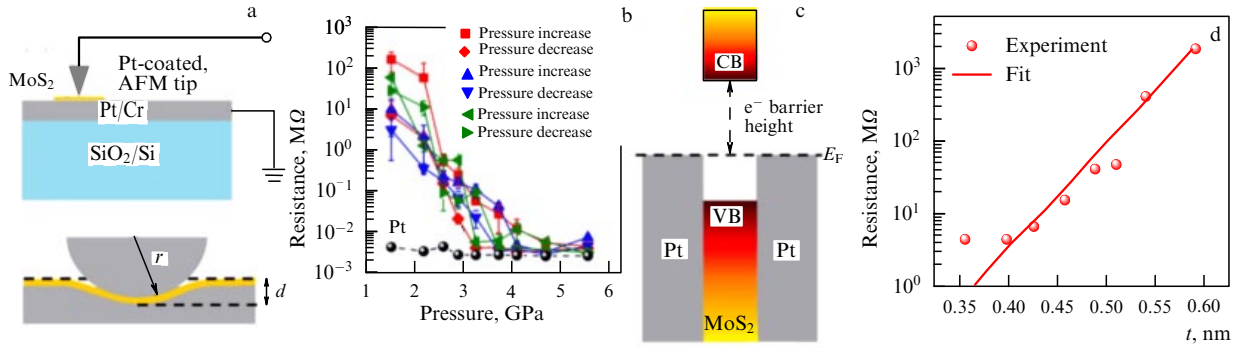

Figure 18. (Color online.) (a) Schematic of the setup for measuring tunneling conductivity through an MoS_2 monolayer using an AFM probe and a sketch of the probe contact model showing an elastic sphere of radius r that deforms the film to a depth d. (b) Measured resistance versus applied pressure. For comparison, contact resistance on the surface of a Pt electrode without the MoS_2 monolayer is also shown. (c) Band diagram of the MoS_2 monolayer located between two Pt surfaces in equilibrium. (d) Effective resistance versus barrier width [158].

6.1 Tunneling resistance modulations under deformation of monolayers

The development and study of new nanostructured composite materials often lead to the creation of deformed layers that play the role of tunnel-transparent barriers and determine the functional properties of materials. For example, the possibility of tunneling resistance modulation in MoS_2 monolayers using the conducting tip of an AFM was demonstrated in [158]. The resistance between the conducting AFM tip and the bottom electrode separated by an MoS_2 monolayer was studied, as shown in Fig. 18. The sharp tip allows applying pressures of several GPa, under which the resistance of the MoS_2 monolayer is reversible and changes exponentially by three to four orders of magnitude. A significant change in resistance is explained by quantum tunneling, when the thickness of the MoS_2 monolayer is modulated by the tip. A defect-free MoS_2 monolayer can serve as an active layer for nanoelectromechanical switches. Double-layer and few-layer MoS_2 also showed a change in resistance by 2 to 3 orders of magnitude under voltage modulation, but with a higher resistance for the 'on' state, which is less attractive for applications than is single-layer MoS_2. The authors suggest that, in addition to MoS_2, any high-quality 2D semiconductors (monolayers such as WS_2 and $MoSe_2$) can also be used as a material for switches.

6.2 Locally deformed films: deformation-related effects and possible applications

Different approaches are used to produce locally deformed films (Fig. 19): monolayers transferred onto nanopillars [159] and onto closely packed SiO_2 nanospheres of different diameters [160], and monolayers with folds, blisters, or a combination of them [161, 162]. The average deformations that arise, for example, depending on the diameter of SiO_2 nanospheres, change several-fold. If the corrugation elements are high and sharp, then most of the graphene is suspended and does not interact with the substrate; on the other hand, if the substrate relief is smooth, then the graphene–substrate interaction is uniform and weak. Therefore, it is most desirable to have spatially bound corrugated substrate elements with a small curvature radius (for example, small arrays of nanospheres) such that graphene is mostly attached to the substrate but has sufficiently strong inhomogeneities, so as to be subject to locally nonuniform deformation. This design principle can be applied not only to graphene on SiO_2 but also to all other 2D materials on various substrates.

Various approaches to the creation of periodically deformed structures from different 2D materials are discussed in review [163]. In Fig. 19d, we show the work of

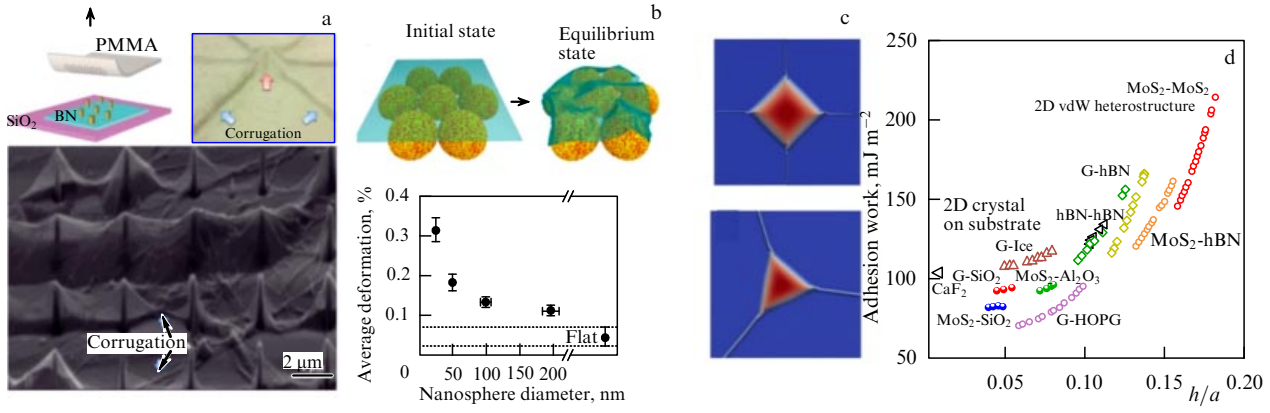

Figure 19. (a) Graphene transfer onto nanopillars and optical image of the obtained structures [159]. (b) Schematic representation of graphene deposited on monolayers of hexagonal close-packed SiO_2 nanospheres of different diameters, and average deformations that occur depending on the nanosphere diameter [160]. (c) Atomic force microscopy of blisters and folds on the surface of graphene [161, 162]. (d) Values of adhesion work for different interfaces of a 2D material in heterostructures depending on the aspect ratio of blisters [164]; h and a are the height and size of the blister, vdW are van der Waals heterostructures.

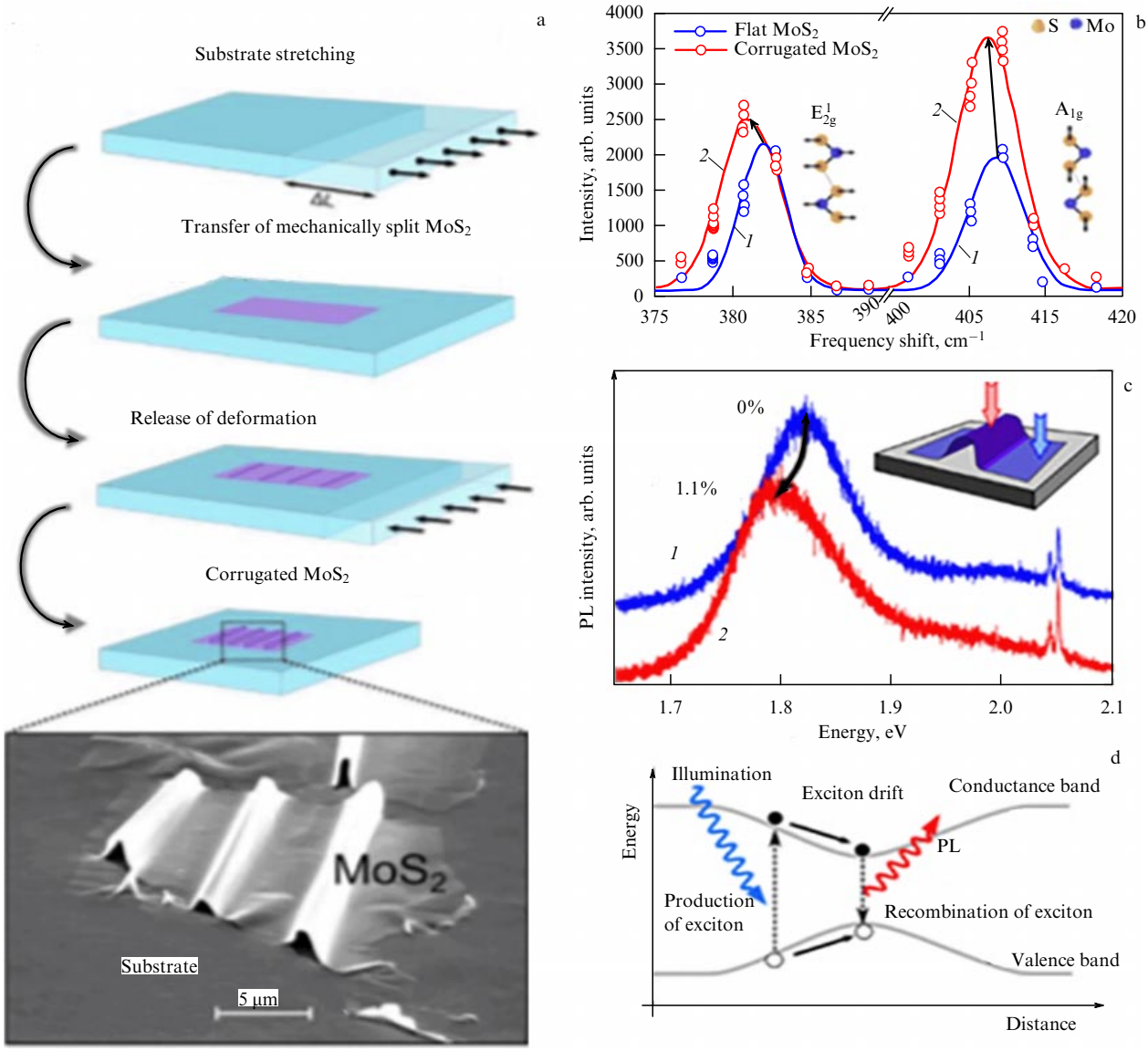

Figure 20. (Color online.) (a) Schematic diagram of the fabrication of folded nanolayers. Elastomeric substrate is stretched prior to the application of the 2D material; the substrate is then released, which causes the formation of folds. Image of the resulting MoS_2 layers. (b) Raman spectra measured on the flat (blue line *1*) region of the MoS_2 layer and on a fold (red line *2*). Shift of the E^1_{2g} and A_{1g} peaks toward lower frequencies is shown. (c) PL spectra measured on a flat region (blue) and on the top of a fold (red) in the same MoS_2 particle. (d) Schematic diagram explaining the 'funneling' effect due to nonuniform deformation in the region of MoS_2 folds [171].

adhesion for various material–substrate 2D systems considered in [164]. These results show that deformations in 2D materials rely on the properties of interfaces, and primarily on adhesion, defining the fundamental principles for designing mechanical deformations in 2D materials and heterostructures for modern applications.

The frequency shifts of the Raman spectra peaks in 2D materials under deformation allow using this dependence for studying local deformations. For example, folds formed in CVD graphene due to the difference between the thermal expansion coefficients of graphene and copper substrate have been analyzed theoretically from the standpoint of local deformations introduced by them [165] and from the standpoint of engineering based on the use of these deformations [166]. It was shown theoretically that the magnitudes of deformations vary several-fold, depending on the method of connecting the folds to each other. On the other hand, the rate of shift of the 2D Raman spectra peak in the region of folds has been determined experimentally in the range of 25–30 to 60–70 $cm^{-1}/\%$ [167]. The difference is due to the geometric size of the fold grid. In addition, blisters (or nanobubbles) can form arbitrarily or in a controlled manner in 2D materials due to various causes and can be used to alter the properties of these materials [168]. The principal mechanisms of formation, evolution, and destruction of folds have been discussed in numerous studies, which can lead to the understanding of these phenomena at the atomic level and provide guidelines for the introduction of folds in graphene for specific applications [169, 170].

As we have noted, controlling the band structure by locally deformed 2D layers is an important approach to tuning the optoelectronic properties of materials at the nanolevel. Atomically thin materials are particularly well suited for this purpose, because they can withstand extreme

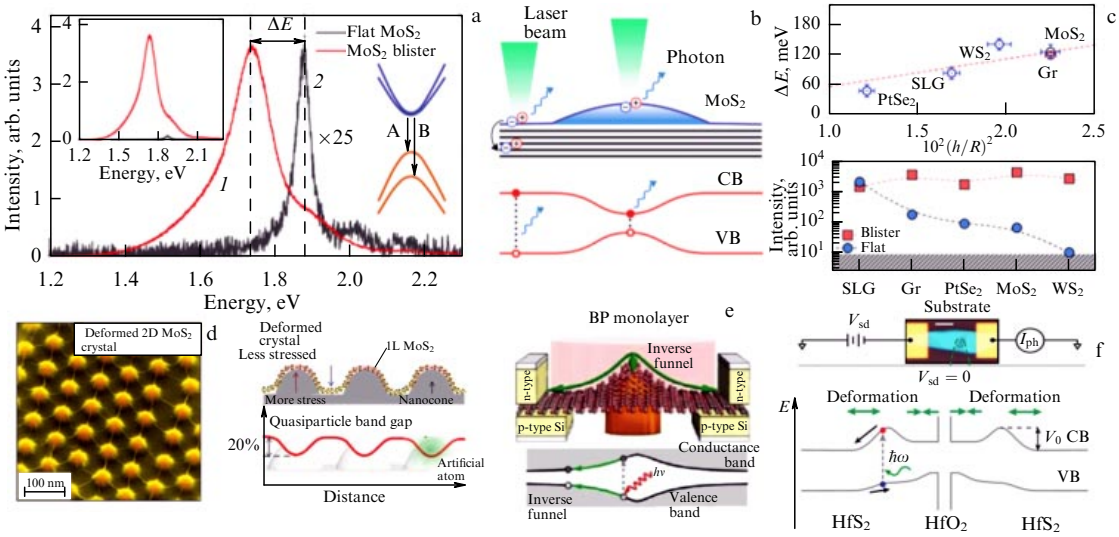

Figure 21. (Color online.) Photoluminescence from MoS_2 blisters. (a) PL spectra from a blister (red, *1*) and from a flat region (black, *2*) measured at room temperature on a graphite substrate. Spectral intensity from the flat region is 25 times lower than the intensity from the blister. Left inset: unnormalized PL spectra. Right inset: diagram of the MoS_2 band structure. (b) Blister sketch and band gap profile along the blister. CB and VB denote the conduction band minimum and the valence band maximum. (c) Shift ΔE of the PL peak from MoS_2 blisters as a function of $(h/R)^2$ for different substrates relative to the PL peak for undeformed MoS_2 on h-BN and PL peak intensity measured on flat regions (blue dots) and on blisters (red squares) for MoS_2 on different substrates. Gray area indicates the noise level in PL measurements [172]. (d) Superlattice constructed by introducing local and periodic deformation into the MoS_2 monolayer by forming nanocones in the substrates [173]. (e) Change in the band gap of black phosphorus due to local deformation [175]. (f) Charge funnel effect in devices constructed using HfS_2/HfO_2. Schematic diagram of the range of the device subject to deformation caused by local oxidation of the central part (see inset) [175].

nonuniform deformations before being ruptured. The idea of a 'funnel' (or a mesoscopic artificial atom) was realized in [171], where the effect of local deformations in the region of folds on the electronic band structure of atomically thin MoS_2 was considered (Fig. 20). Photoluminescence imaging allows observing the deformation-induced decrease in the direct band gap and the change in the spectrum of photoproduced excitons in the region of higher deformations.

Nonuniform uniaxial deformation produced by creating folds was also used to modify the $ReSe_2$ band structure [148]. In that study, the effect of deformation on the electrical and magnetic properties of $ReSe_2$ was investigated using the fold method. The formation of folds was shown to be attended by a red shift of the Raman and PL peaks in the spectra and a change in the conductivity of the material with folds.

The ability to adapt the PL of single-layer transition-metal dichalcogenides using deformation is of considerable interest for optoelectronic applications. It was shown in [172–174] that the use of nonuniform deformations and the creation of 'artificial atoms' lead to the formation of a funnel for excitons. Creation of hydrocarbon-filled MoS_2 blisters on an atomically flat substrate results in controlled localized PL from different submicrometer regions. The energy of radiation of such structures is determined by the built-in deformation and can be controlled by the choice of the substrate material (Fig. 21). As a result, both the maximum deformation and the deformation profile are universal for all blisters on a given substrate, regardless of their size. It was shown that, for blisters formed by a MoS_2 monolayer, the PL can be tuned in the range of 1.72–1.81 eV by choosing bulk $PtSe_2$, WS_2, MoS_2, or graphite as the substrate, and the PL intensity is significantly enhanced by the 'funnel' effect. PL quenching in regions of good contact between the MoS_2 monolayer and the substrate ensures the localization of the glow only in blisters. For other compounds (black phosphorus, HfS_2), deformations lead to a local increase in the band gap (Fig. 21e, f) [173–176]. This also allows designing structures with a modulated band gap and local regions of enhanced PL. The proposed approach thus opens prospects for the creation and study of light-emitting 'artificial atoms' for use in specific applications.

A theoretical model of the effect of deformation on the charge distribution and its transfer to graphene (deformations out of the graphene plane) is presented in [177] in terms of scalar and pseudomagnetic fields that control the electron dynamics. Two different geometries, a blister and a fold, are chosen to represent the deformations observed most commonly under experimental conditions. It is shown that local charge accumulation regions with a peculiar charge distribution form inside the deformed regions, contributing to the population of only one sublattice (K or K′). Under certain conditions, resonant states are observed in localized charged regions, which gives rise to the presence of discrete levels in the band structure. This is similar to the bounds created by potential barriers. In addition, electron currents through the stressed regions are spatially separated into their valley components, which allows manipulating electrons with different valley indices. A double-fold structure can be used, where the first fold acts as a polarizer and the second as a detector of electrons in different valleys.

Deformation can help control the charge density distribution at the sublattice level or globally in the deformed region. Localized states that determine the transport properties of graphene can arise in graphene folds. For example, electron–electron interactions usually do not manifest themselves in graphene, but they can become dominant in deformed graphene [178, 179].

Interesting transport phenomena can also be studied from the standpoint of the interaction between an external magnetic field and the deformation-induced pseudomagnetic field [180]. Because the external magnetic field has the same effect on the

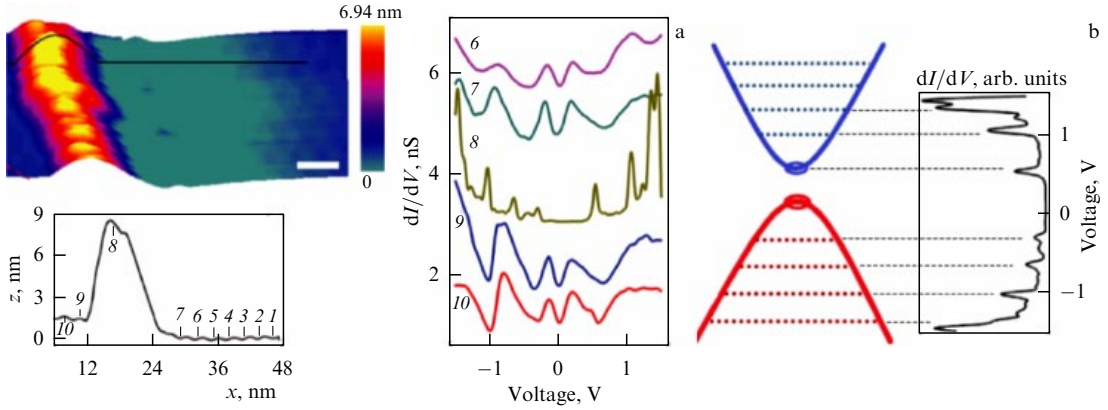

Figure 22. (a) STM image of a graphene bilayer with a fold developed along an Rh foil step. White strip shows the size of 5 nm. Rotation angle of two-layer graphene is approximately 5.1°. (b) STS measurements at different points along a line drawn across the fold [189].

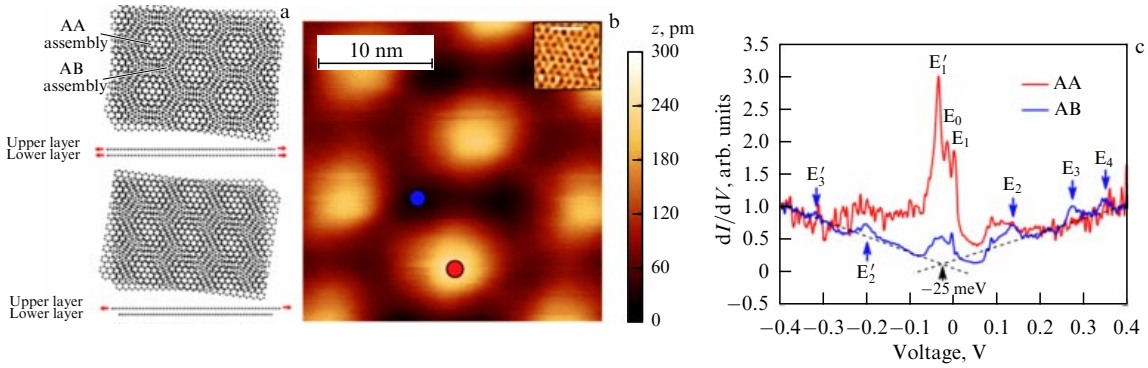

Figure 23. (Color online.) Unfolded and stretched tense structures. (a) Graphene layers and sketches of structures created without deformation (upper diagram) or with deformation (lower diagram). Red arrows in the side views show deformation in each layer. (b) STM image of unfolded graphene layers, 26.4 × 26.4 nm in size. (c) Differential conductivity measured at the marked points in Fig. b (red and blue lines for the respective AA and AB regions show multiple resonances in the AA regions and broad peaks at higher energy in the AB regions) [190].

two valleys, but the pseudomagnetic field has opposite effects, the balance between the electrons in the valleys is violated. The electrons from different valleys can be filtered by applying an external magnetic field of the same magnitude as the constant pseudomagnetic field in triaxially deformed graphene, where the magnetic field is compensated for electrons in one valley, and electrons in the other valley experience the magnetic field equal to twice the external field [180].

6.3 Combining deformation and layer rotation in bilayer structures

To control the functional properties of materials, it is interesting to combine deformation with other adjustable factors, for example, moiré patterns in bilayer structures [181, 182]. It was proposed recently that the effect of interlayer coupling on electrons in twisted two-layer graphene can be understood in terms of the appearance of pseudomagnetic fields [183, 184]. Interesting effects can be expected in the presence of pseudomagnetic fields arising from both deformation and moirée patterns. Recent studies of unfolded layers of bilayer graphene have shown that deformation can increase the separation of the conduction and valence bands and can also determine a lower bound for the Fermi velocity [181].

It is well known that the band structure of a graphene bilayer is strongly affected by the type of structure of these layers and especially by the mutual rotation of the layers (see, e.g., [185, 186]). It has been shown theoretically and experimentally that, when rotated through the so-called magic angle at low temperatures, bigraphene become superconducting [187, 188]. The magic angle is the one at which the Fermi velocity in the material decreases to zero as a result of the formation of a flat zone and the appearance of strong electron–electron interactions. In bilayer graphene, the first magic angle is close to 1.1°.

The deformation-induced evolution of the local electronic properties of a graphene bilayer with unfolded layers (at the rotation angle of 5.1°) was studied by scanning tunneling microscopy and spectroscopy (STM and STS) in [189]. As a result of the rotation, a superlattice is formed in the graphene-on-graphene bilayer, which determines the local band structure (Fig. 22). The folds of the bilayer introduce local deformations of the lattice, which at a zero magnetic field results in effects that simulate the quantization of massive chiral fermions of two-layer graphene with a Bernal lattice in a perpendicular magnetic field of about 100 T along the strained fold. In addition, deformation leads to the appearance of a significant energy band gap at the neutrality point. The sharp peaks on curve *8*, the authors believe, are associated with the Landau quantization of a stressed graphene bilayer in a strong pseudomagnetic field.

By not only rotating the layers relative to one another but also stretching them independently of each other, a certain difference can be created between the periods of the crystal lattices of the layers [190]. Graphene layers were considered to be rotated through 1.25° relative to each other. The structures

were created from graphene grown on SiC and the deformed top layer. The stretching deformation in the experiment was 0.35%. The authors of [190] note that the layers can be stretched independently of each other in two-layer graphene, because they are interconnected not by a covalent bond but by a relatively weak vdW interaction. The resulting structures and the results of their measurements are shown in Fig. 23. As in the case of undeformed two-layer graphene, regions of regular alignment of two layers alternate in the formed structure with regions where the layers are shifted relative to each other by half a period; such regions, however, do not form a hexagonal lattice but a more complex one. As a result, uniaxial heterodeformation suppresses Dirac cones and leads to the appearance of bands with different properties (AA and AB) in the unfolded graphene layers. The differential conductivity, which is proportional to the local DOS in regions AA and AB, was measured at $T = 50$ mK; it is shown in Fig. 23c. Interestingly, the heterodeformation of the structures does not suppress the electron localization caused by moiré formation. The most important feature of the measured characteristics of heterodeformed structures is the presence of a group of resonances (E_1', E_0, and E_1) located near zero energy. An additional analysis is required to understand the nature of the observed peaks; however, the results obtained demonstrate new possibilities for directed changes in the properties of vdW structures.

The critical parameter in bigraphene structures is the interlayer adhesion strength, which can be tuned in a controlled manner by changing the interlayer separation in vdW heterostructures using hydrostatic pressure. It was shown in theoretical paper [191] that the effect of a hydrostatic pressure of about 2 GPa on bigraphene layers rotated through a small angle allows increasing the magic angle to 1.5° (instead of $\sim 1.1°$) due to enhanced tunneling between layers. Such layers have a significantly greater structural resistance to moiré deformations and have a finer moiré pattern.

Combining hydrostatic pressure with controlled rotation of layers in bilayer structures provides opportunities for dynamical control of the bilayer band structure. For example, in devices where bigraphene is encapsulated by boron nitride, an increase in pressure applied to the moiré superlattice leads to an increase in the band gap width [192]. Theoretical modeling demonstrates the significant role played by atomic-scale structural deformations and reversible changes to the band structure by hydrostatic compression.

It has been shown theoretically that current-voltage characteristics in zigzag graphene nanoribbons can feature a negative differential resistance caused by quantum selection rules [193]. The magnitude of the effect depends on the type and direction of the applied deformation: for a stretching deformation along the ribbon axis, the on/off ratio increases, while for compressive deformation, the negative differential resistance gradually disappears. This property can be useful for a nanoelectromechanical switch. In addition, under an oblique uniaxial deformation, a transverse current arises between the upper and lower edges of the nanoribbon.

6.4 Self-assembly of foreign atoms on the surface of graphene using deformations

Surface adsorption of foreign atoms is regarded as a promising way to tune the electronic and chemical properties of graphene and other 2D materials [194, 195]. In particular, the hydrogenation of graphene is an elegant way to open the graphene band gap and has been extensively studied both experimentally and theoretically [196–198]. However, placing hydrogen atoms or other atoms and molecules in the right places inside graphene is not easy. Deformation engineering will hopefully be a promising way to promote the self-assembly of adsorbed atoms on graphene [199]. In the case of deformations, a relief appears on the surface, and locations with a higher curvature become more chemically active [200] and act as preferable sites for the adsorption of impurities. Figure 24 illustrates this idea as expounded in [201]. For a uniaxial compressive strain exceeding a certain critical value ε_{cr}, a flat graphene sheet becomes undulating. Based on the continuum mechanics model [202], this critical strain can be calculated as $\varepsilon_{cr} = (hn\pi)^2/12(1-\nu^2)L^2$, where h is the

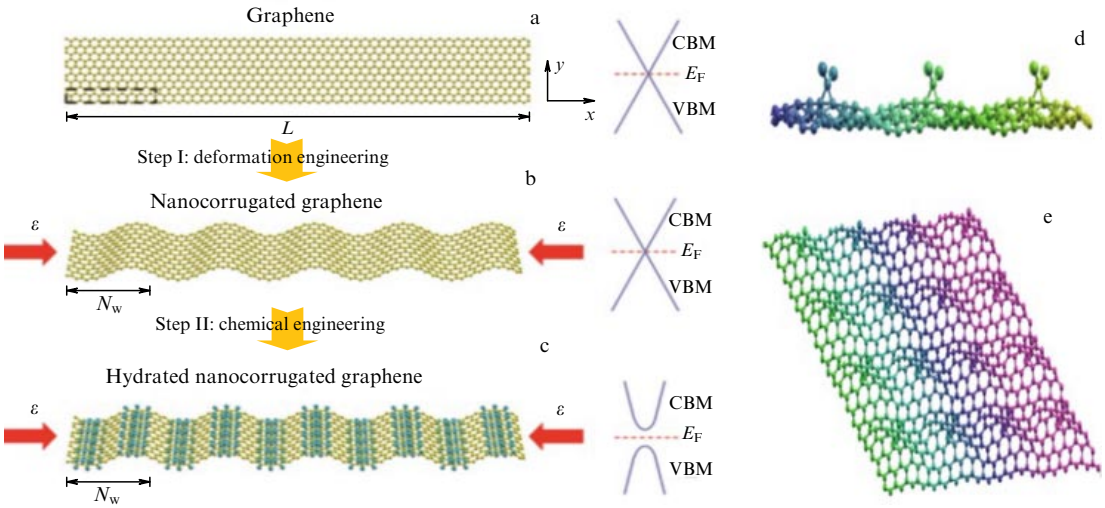

Figure 24. Schematic representation of the process of self-assembly of hydrogen atoms on graphene by the deformation method. (a) Initial graphene with zero band gap; L is the sample length. (b) Nanorelief formed by compressive deformation of graphene, which remains semimetallic; N_w is the nanorelief period. (c) Adsorption of hydrogen atoms on bent graphene. After the adsorption of hydrogen, a band gap opens. CBM, VBM, and E_F denote the conduction band minimum, the valence band maximum, and the Fermi level [201]. (d, e) Physical model of self-assembly of halogenated layers of carbene (divalent carbon compound) on graphene: corrugated structure corresponding to the adsorption of CCl_2 molecules in the armchair direction [210].

graphene thickness, n is the number of waves, and $\nu = 0.34$ is Poisson's ratio. For graphene size $L \sim 10$–10^4 nm, the critical strain ε_{cr} is extremely small ($< 0.1\%$) [29]. The wave period is modulated by the graphene length and compression deformation. Hydrogen atoms are adsorbed on carbon atoms with the highest curvature, forming a highly ordered functionalization of graphene (Fig. 24c). Carbon atoms are more reactive in the locations of bends, because, instead of the electronic sp^2 configuration in planar symmetry, the C atom acquires the $sp^2 + \delta$ configuration, which is closer to sp^3. Therefore, less energy is required for adsorption in curved regions than in flat regions. The formed functionalized bands separate the graphene ribbon by potential barriers and lead to the band gap opening. Similar effects can be observed under the functionalization of graphene with fluorine [203, 204] and other atoms and molecules.

Thus, in addition to the ability to control the surface nanorelief and hence the band gap width, it became possible to control the process of adsorption and desorption of impurity atoms and the reversible metal–semiconductor–metal transition. Similar nanorelief structures were realized experimentally for graphene on a prestretched elastomeric substrate [205–207].

This idea also applies to the self-assembly of other atoms such as F, Cl, and O on graphene. If epitaxially grown graphene is oxidized using atomic oxygen in an ultrahigh vacuum, then the inevitable formation of a nanorelief results in the adsorbed O atoms preferring to occupy certain regions with the highest local curvature [208, 209]. Folds that form during the growth of graphene on copper and remain after the transfer to another substrate, as well as folds artificially formed in a 2D material, act similarly.

A physical model for the self-assembly of CCl_2 molecules on graphene was proposed in [210]. The self-assembly of the adsorbed layer was shown to be determined by a combination of the curvature of the graphene sheet, local distortions introduced by molecular adsorption, and intermolecular repulsion at short distances. The thermodynamics of bivalent covalent molecular adsorption and the resulting electronic structure have been calculated using the DFT. A direct band gap was shown to open with a width that can be tuned by changing the coating. This provides a mechanism for designing the electronic structure of graphene and hence its use in semiconductor technologies.

7. Deformation-related effects in heterostructures made of 2D materials

Heterostructures play an important role in modern semiconductor devices and in many applications of micro and nanosystems in electronics and optoelectronics. The most intriguing frontier of modern heterostructures is the structures of monoatomic layers. Deformation engineering of materials and heterointerfaces is currently regarded as a way to adjust (modify) electron states, energy bands, and functional properties of heterostructures, which helps in the discovery of new physical phenomena or new applications of 2D heterostructures [37].

Monolayer strained heterostructures (InAs(1ML)/GaAs(1ML)) were first produced back in 2000 [211]. Lattice mismatch stress in such heterostructures has been used to self-form various structures with 3D shapes: nanotubes, spirals, corrugated films, hemispheres, etc., with bending radii down to 1 nm [212]. It was shown that the elasticity theory is applicable to these heterostructures with a thickness of several monolayers, which allowed calculating the change in the band gap under the action of deformation. Changes in the band gap width in multilayer nanotubes and in periodically compressed and stretched layers of nanocompressed structures were given in [212, 213]. Huge changes in the band gap width, up to 0.8 eV, and quantum processes lead to the formation of fundamentally new structures important for applications. Stressed structures can shape graphene and other 2D materials [214].

Lateral heterostructures based on graphene and graphane ribbons (hydrogenated graphene) were considered in [215]. Band gap opening is predicted theoretically, with the width oscillating with a change in the distance between graphane chains. An interesting possibility is the creation of a band with quasimetallic conductivity enclosed by graphane ribbons with a large band gap (an electron waveguide). Moreover, it has been shown that the nanoribbon band gap can vary by up to 30% due to mechanical stresses directed across the graphane ribbons.

7.1 Mutual influence of layers in heterostructures on their mechanical properties

When using the layer transfer process to produce vdW heterostructures, the question arises as to whether a strong interlayer interaction is present in such structures. Mechan-

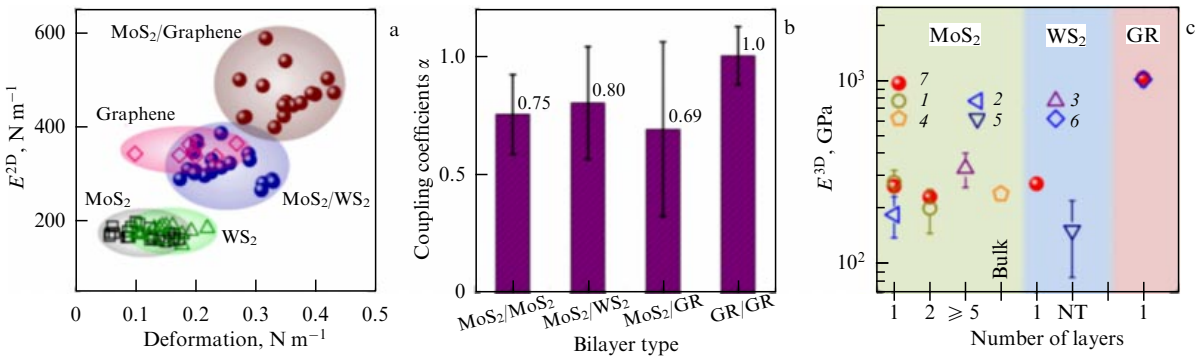

Figure 25. Comparison of elastic properties of different 2D layers. (a) Experimental data for the elastic modulus depending on initial deformation of various 2D layers and heterostructures. (b) Coupling coefficients for different types of bilayers. (c) Comparison of Young's modulus of homo- and heterostructures with the moduli of multilayer films and bulk materials taken from the literature. NT: nanotubes. Elastic moduli of the layers were measured using an AFM tip on a suspended circular membrane [59]. *1* — [216], *2* — [218], *3* — [217], *4* — [219], *5* — [220], *6* — [32], *7* — [59].

Table 3. Mechanical properties of monolayers and heterostructures. G: graphene, M: MoS_2. E is Young's modulus normalized to the monolayer thickness (0.345 nm for graphene and 0.609 nm for MoS_2), D is the bending modulus, $\sigma_{max}^{3D} = \sigma_{max}^{2D}/h$ is the tensile strength, where h is the layer or structure thickness, ε_{int} is the fracture deformation [221].

Structure	E, GPa		D, eV		σ_{max}^{3D}, GPa		ε_{int}, %	
	Theory	Experiment/ reference	Theory	Experiment/ reference	Theory	Experiment/ reference	Theory	Experiment/ reference
G	1050	1000 [32]	1.2	1.17 [224]	214	125 [32]	19	25 [32]
G/G	1060	1040 [226]	54.8	35.5 [223]	237	128 [226]	18	25 [226]
M	160	270 [222]	8.5	9.6 [226]	36	25 [222]	10	6 [222]
M/M	270	200 [222]	73.5		30	23 [222]	6	11 [222]
G/M	530	490 [59]	120.6		128		15	
M/G	520		113.1		116		15	
G/M/G	680	560 [119]	726.9		136		10	
M/G/M	450		698.4		100		14	

ical measurements can determine the coupling between layers [59]. Figure 25 shows the results of measuring Young's moduli of individual monolayers and heterostructures based on them, as well as the layer coupling coefficient. If there is no interaction between the layers, the upper layer can freely slide over the lower one, and the measured Young's modulus of the two-layer structure is determined only by the lower layer, which is fixed on the substrate. None of the monolayer heterostructures studied in [59] demonstrates slip. The measured Young's modulus of a two-layer heterostructure can be phenomenologically described as $E^{2D} = E_{bottom}^{2D} + \alpha E_{top}^{2D}$, where α is the layer coupling coefficient, which ranges from 0 to 1. Comparing Young's moduli of the heterostructure with the sum of those for monolayers, we can estimate the layer coupling coefficient, which turns out to be close to unity.

Transition-metal dichalcogenides such as MoS_2 are layered semiconducting materials that are promising for applications in flexible electronics, but their low mechanical strength (see Table 1) is an obstruction to their practical use. Both two- and three-layer heterostructures formed by MoS_2, supported or encapsulated by graphene, were considered in [221]. Mechanical properties such as Young's modulus, the flexural modulus, the maximum tensile stress, and the breaking strain are extracted from nanoindentation and compared with single-layer and homogeneous two-layer systems. The simulation results and their comparison with known experimental data are given in Table. 3. Regardless of the order of assembly, the heterostructures turn out to be mechanically more stable than mono- and two-layer MoS_2, mainly due to the mechanical reinforcement provided by the graphene layer. The maximum tensile stress and breaking strain values are the same for two- and three-layer heterostructures and are significantly higher than for mono- and two-layer MoS_2. These results demonstrate the potential of graphene-based heterostructures to improve the mechanical properties of transition-metal dichalcogenides.

Heterostructures made of a layer of silicene placed between two layers of graphene were studied theoretically in [227]. The maximum stress and Young's modulus of heterostructures increase by about an order of magnitude compared to the corresponding parameters of silicene. Thus, the use of heterostructures to strengthen monolayers of various 2D materials is very promising for the design of flexible electronics.

Van der Waals heterostructures made of MoS_2 and graphene monolayers are amenable to experimental studies of the interaction between semiconductor and semimetallic 2D materials [228]. As a result of the interaction between layers, a redistribution of electrons in heterostructures is observed, which leads to a shift of the Dirac point and the peak positions in Raman spectra. The A_{1g} peak position (MoS_2) is shifted by 0.7 cm^{-1} toward higher frequencies (blue shift), and the G peak, associated with graphene, by about 7 cm^{-1} toward lower frequencies (red shift). The Fermi level of G/MoS_2 vdW heterostructures is higher than that of the original graphene, which suggests a decrease in the concentration of holes in graphene and a displacement of the Fermi level toward the Dirac point due to the transfer of electrons from MoS_2 to graphene. In $BN/G/MoS_2$ structures, the presence of the h-BN layer increases the Fermi level of graphene (from -267 to -188 meV for the graphene Dirac point and from -209 to -140 meV for graphene/MoS_2 structures), indicating that the insulating coating reduces p-type doping effects.

7.2 Effect of deformation on the electronic spectrum and properties of heterostructures

At present, 2D materials are being actively studied as the basis of flexible electronics. We note that heterostructures belong to the area where the understanding of the effect of mechanical stresses is still somewhat limited. Such an understanding of the effects associated with deformation is especially important for instrumental devices of nanoelectronics made of 2D materials in which significant mechanical deformations can be built in constructively. Using Kelvin probe microscopy, the effect of uniaxial stretching on graphene/WS_2 (mono- and multilayer) heterostructures was studied in [229]. The work function of both graphene and WS_2 in graphene/WS_2 heterostructures was found to increase with deformation. This corresponds to efficient deformation transfer between graphene and WS_2, which indicates a strong vdW interaction, charge transfer efficiency, and mechanical stability of the heterostructures. The increase in the work function is presumably associated with p-doping of materials due to the charge transfer between the layers and the organic substrate (polyethylenenaphthalene) and the corresponding decrease in the position of the Fermi level.

The effect of normal compressive deformation on the electronic and mechanical properties of MoS_2 multilayer and MoS_2/graphene heterostructures was studied using the DFT in [222, 230]. An example of the experimental implementation of the normal compressive deformation can be seen in Fig. 18; theoretically, this was done by decreasing the distance between layers. It was shown (Fig. 26) that, due to a strong dependence of the band gap width of multilayer MoS_2 on the

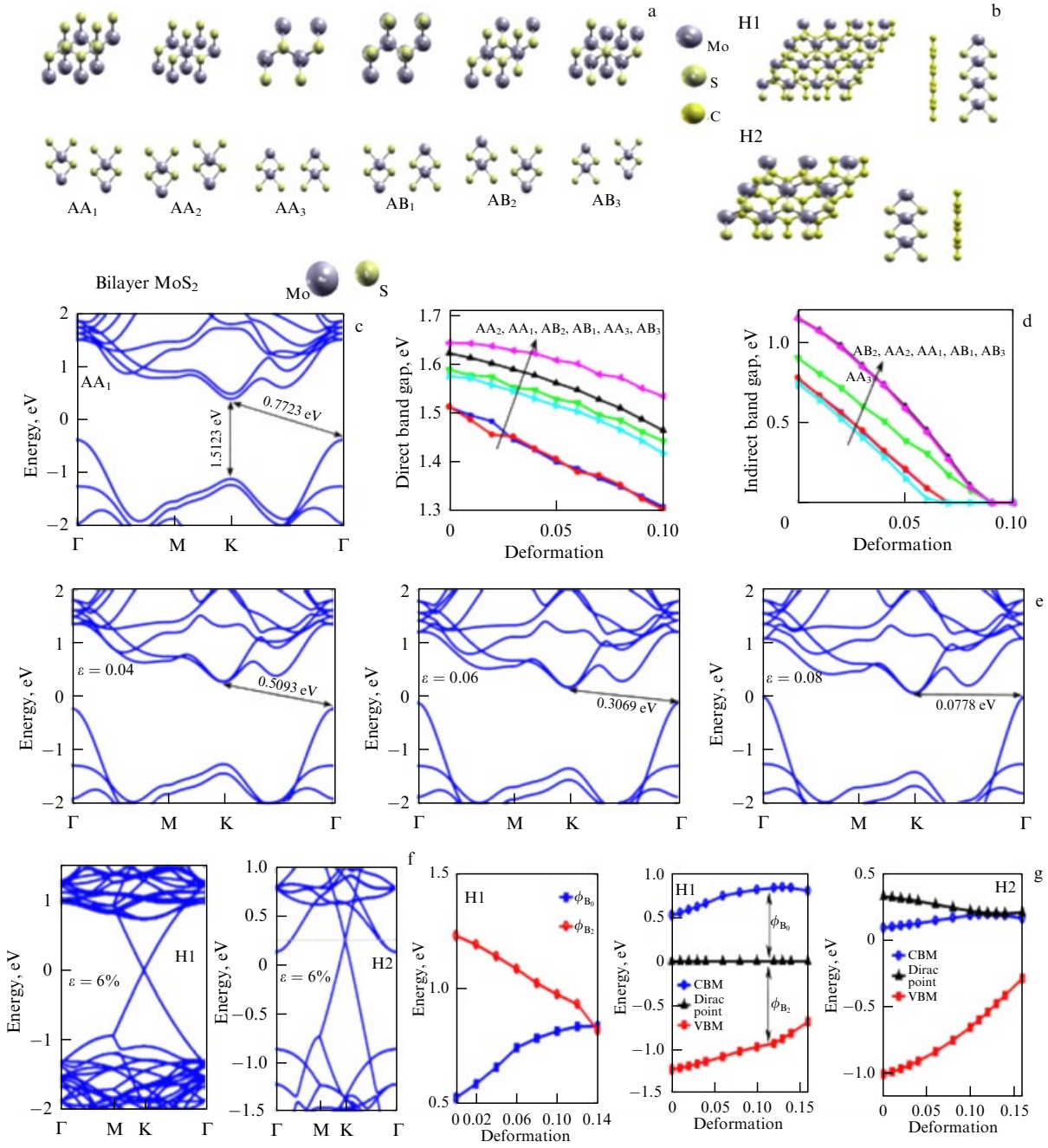

Figure 26. Alterations in the band structure at normal pressure for MoS_2 bilayers and MoS_2/graphene heterostructures. (a) Top view and side view for different atomic structures of MoS_2 bilayers. (b) Top and side views of supercells H1 (5×5 graphene/4×4 MoS_2) and H2 (4×4 graphene/3×3 MoS_2). (c) Band structure of one of the AA_1 bilayers in the absence of external pressure. (d) Change in the width of the direct and indirect band gap of an AB_1 bilayer as a function of the applied strain. (e) Band structure of the AB_1 bilayer under 4%, 6%, and 8% deformation. (f) Band structure of H1 and H2 heterostructures under 6% deformation. (g) Changes in the ϕ_n and ϕ_p barriers, the position of the Dirac point for graphene, the valence band maximum (VBM), and the conduction band minimum (CBM) for MoS_2 in H1 and H2, depending on the deformation [223, 230].

normal compressive deformation, a semiconductor-to-metal transition can occur. For two-layer structures, the transition occurs at a 6.2–8.7% deformation; the minimum deformation was obtained for the AB_2 bilayer (see Fig. 26) due to the minimum distance and the strongest interaction between the sublayers in that structure. The change in the band gap width is reversible, and when the deformation is removed, the structure returns to its original state. This makes heterostructures promising for sensor applications. Two different MoS_2/graphene heterostructures with different numbers of cells were studied. The first heterostructure, H1, exhibits stretching deformation by 1.66% in the graphene plane and compressive deformation by 1.75% in the MoS_2 plane. In the H2 structure, the graphene plane was compressed by 0.24%, and the MoS_2 plane was stretched by 2.81%. We note that graphene structures on the MoS_2 substrate demonstrate a high carrier mobility, about 60,000 $cm^2\ V^{-1}\ s^{-1}$ [224, 231], making MoS_2 a promising substrate for graphene. In addition, as shown above, graphene/MoS_2 heterostructures exhibit excellent mechanical properties due to the presence of graphene [221]. The graphene/MoS_2 band structure is a combination of the band structures of graphene and MoS_2,

and a linear dependence of dispersion for graphene at the Dirac point is preserved in the heterostructures. The direct and indirect MoS_2 band gap width can be controlled in heterostructures by normal compressive deformation, and in the second heterostructure the band gap is smaller due to the stretching of MoS_2. The band structure in H1 turned out to be strongly dependent on the normal compressive deformation, which changes the distance between the layers, the barrier height, and the charge transfer between graphene and MoS_2. In H1, the minimum of the conduction band and the maximum of the valence band move upward, which increases the n-type barrier and reduces the p-type barrier. At a normal compression deformation of more than 13%, the MoS_2 band gap becomes indirect, and, at a deformation level of 13.5%, the heterostructure changes the bending of the bands from the n-type Schottky barrier to the p-type.

In H2, the Dirac point of graphene is located above the conduction band minimum; this means that, when a stretching deformation is applied to MoS_2, a semiconductor-to-metal transition occurs. As the compressive deformation in H2 increases, the Dirac point of graphene moves downward due to charge transfer between layers; more and more electrons therefore go from MoS_2 to graphene. We note a discrepancy between the results of theory and experiment [123] in predicting the band gap width, which is due to an underestimation of the band gap width calculated using the DFT. Nevertheless, the general tendency describing the effect of normal compressive deformation coincided with the experimental results. Similar results were obtained in modeling MoS_2/graphene transistor heterostructures [225, 232], where it was shown that the band gap width can be changed by varying the distance between graphene and MoS_2 by applying deformation or gate voltage.

Nanomechanical devices based on MoS_2/graphene vdW heterostructures were created and studied in [230, 233]. By transferring an MoS_2 monolayer onto suspended layers of graphene (one to four monolayers in thickness), heterostructures can be obtained that exhibit stable nanomechanical resonances in the high-frequency range (up to $\sim$ 100 MHz). The resonance frequencies of the fundamental mode of heterostructures are between the values for graphene (50–120 MHz) and MoS_2 devices (20–60 MHz). The Q-factor of the obtained resonators is lower than that of graphene, but is comparable to the Q-factor of devices based on MoS_2, which is presumably associated with a strong interlayer interaction in vdW heterostructures. Suspended structures are in a stretched state, and the resonance frequencies of heterostructures compared to those for graphene and MoS_2 are determined by the level of stretching. Hence, in the case of strong interlayer interaction, suspended heterostructures with mechanically coupled atomic layers are promising for use in nanomechanical systems.

A high-sensitivity deformation sensor based on a variable Schottky barrier in an FET on an MoS_2/graphene heterostructure was proposed in [234]. The low DOS near the Dirac point in graphene allows significantly modulating the position of the graphene Fermi level and the height of the corresponding Schottky barrier in the MoS_2/graphene structure due to deformation-related injection of charge from MoS_2 into graphene. Simulations and measurements of the temperature dependence of conductivity show that the change in the Schottky barrier is maximum if the graphene Fermi level is at the neutrality point, which is achieved by applying a voltage to the gate (an oxide-coated silicon substrate is typically used as a gate). As a result, the maximum change in the Schottky barrier at a 0.17% deformation reaches 118 meV, and the corresponding current change factor is $\sim 10^3$, which leads to an ultrahigh sensitivity of the sensor (current change factor of $\sim 5.7 \times 10^5$). As a result, the sensitivity of deformation sensors based on MoS_2/graphene heterostructures is significantly higher than that of sensors based on Au/MoS_2 (1.2×10^3) and on ZnO (4.0×10^3). The ultra-high sensitivity of FETs with a graphene/MoS_2 channel can be used to develop a range of electronic and mechanoelectronic nanoelectronic devices.

Selective and scalable growth of WS_2 on graphene allows designing WS_2/graphene heterostructures [235]. Based on Raman spectroscopy data, it was found that, after the synthesis of WS_2, graphene undergoes compressive deformation and doping with holes to 10^{13} cm^{-2}. The doping is associated with modification of the SiO_2 stoichiometry on the graphene/SiO_2 interface during the WS_2 growth. Electrical transport measurements show that, at high positive gate voltage, the heterostructure behaves like an electron-blocking layer, making it a suitable candidate for the development of unipolar optoelectronic components.

Another approach to the analysis of the interaction between layers in heterostructures was proposed in [11]. An *in situ* study of the Raman spectra of vertical CVD-grown WS_2/MoS_2 heterostructures subjected to bending revealed a transition from bonded monolayers to the destruction of these bonds and interlayer slip. The Raman spectra shown in Fig. 27 show a jump in the shift in the positions of Raman peaks at a stretching deformation of 1.2%. The conclusion about the slip of the layers is also supported by microscopy data. Thus, a weak interlayer coupling in WS_2/MoS_2 heterostructures has been shown, and the change in the coupling between monolayers under deformation can be directly observed using Raman spectroscopy.

It is known that layers of MoS_2/WSe_2 and $WS_2/MoSe_2$ heterostructures are semiconductors with respective direct and indirect band gaps [236]. The direct band gap in the $WS_2/MoSe_2$ heterostructure can be achieved by applying a compressive deformation of $\sim 0.5\%$. The K point of the valence band then shifts toward higher energies, reducing the band gap width. An important conclusion in [236], that the properties of a heterostructure are typically strongly affected by the order of layers, is supported by many other authors.

When creating lateral heterostructures from monolayers of transition-metal dichalcogenides ($MoSe_2/MoS_2$, $MoS_2/MoSe_2$, WSe_2/MoS_2, and MoS_2/WSe_2), internal deformation occurs as a result of lattice mismatch between layers, which significantly affects their electronic properties [237]. The built-in deformation can decrease or increase the coupling strength between nonmetallic p- and metallic d-orbitals and therefore change the splitting between the bound and antibound states at high-symmetry K points. This has been shown theoretically to result in a relative shift of the band gap edge (up or down) or a shift of the maxima and minima of the states, up to the indirect–direct band gap transitions. The hybridization of states plays an important role in the shift of the band edge, because different 2D materials have different strain resistances. In addition, charge transfer across the heterojunction also affects the band gap width, and degeneracy of band edges can also be violated due to the built-in deformation. In the presence of deformation, the coupling strength of 2D materials in a single

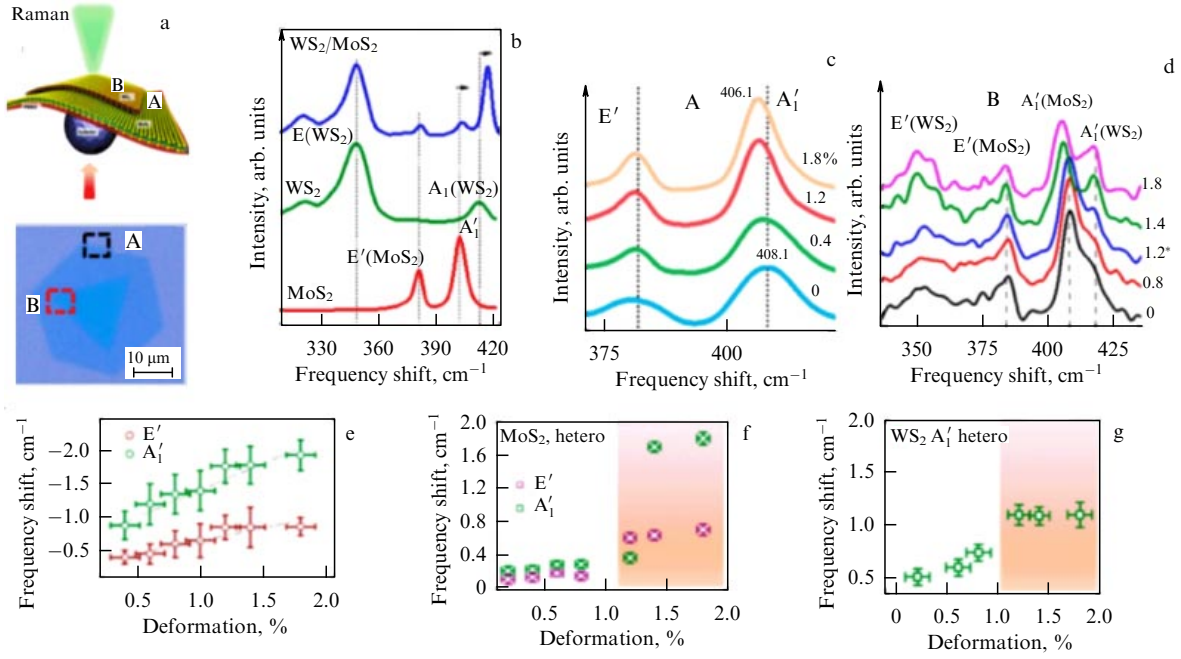

Figure 27. (a) Schematic and AFM images of CVD-grown WS_2/MoS_2 heterostructures. (b) Raman spectra for WS_2/MoS_2 individual layers and heterostructures. (c, d) Raman spectra for an MoS_2 layer (point A) and a WS_2/MoS_2 heterostructure (point B) for different stretching deformations. (e) Change in the spectral position of MoS_2 A'_1 and E′ Raman peaks depending on deformation (at point A). (f) Position changes of A'_1 and E′ bands measured at point B for MoS_2. (g) Changes in the spectral position of A'_1 under deformation for WS_2 [11].

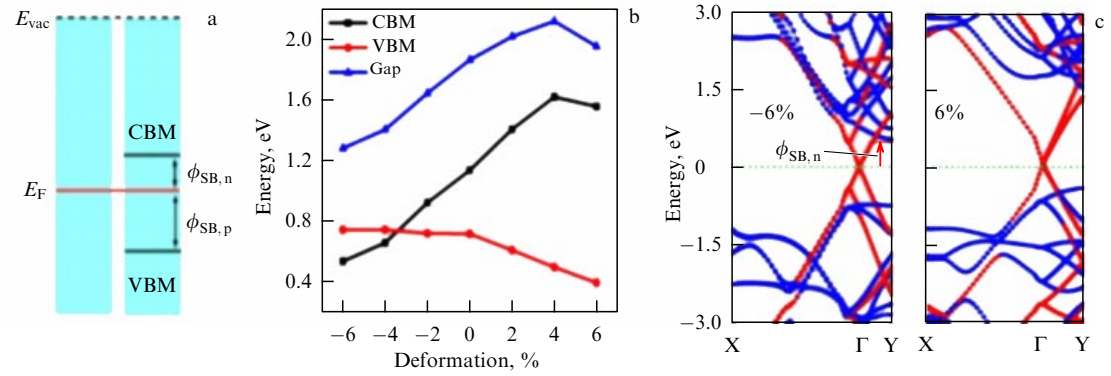

Figure 28. Alterations in the band structure under deformations in the plane of layers of phosphorene/graphene heterostructures. (a) Diagram of phosphorene/graphene heterostructure; VBM: valence band maximum, CBM: conduction band minimum. Heights of the n-type or p-type Schottky barrier are indicated between the conduction band minimum or the valence band maximum of the phosphorus layer. (b) Dependence of the band gap and VBM and CBM shifts on the deformation of the heterostructure. (c) Band diagram of deformed heterostructures [240].

heterostructure decreases. Thus, it has been shown not only for vertical but also for lateral heterostructures that external and built-in deformations determine the band structure, defect formation, and the conductivity of heterostructures.

The absence of a band gap in graphene restricts its applications; therefore, other 2D materials based on group-IV elements with linear Dirac cones, such as silicene, germanene, and stanene, are widely studied [238]. Van der Waals heterostructures help overcome the low mechanical strength of monolayer materials and expand their electronic and optoelectronic applications [239]. For example, a direct band gap has been shown theoretically in MoS_2/stanene heterostructures. During the formation of heterostructures, electrons pass from stanene to MoS_2, which gives rise to an internal built-in electric field. The deformation, which reduces the distance between the layers, noticeably increases the heterostructure band gap and carrier concentration. In addition, the combined effects of the internal and external electric fields can additionally change the band gap width and, if the external electric field is equal in magnitude and opposite in sign to the internal one, the heterostructure restores the Dirac cone.

The structures and electronic properties of phosphorene/graphene heterostructures were studied theoretically by the DFT in [240]. It was shown (Fig. 28) that the individual properties of phosphorene and graphene are preserved due to the weak coupling between the layers. The electronic properties of the Schottky barrier in a phosphorene/graphene heterostructure can be tuned from the p-type to the n-type using in-plane compressive deformations in the range from −2% to −4%. After analyzing the overall band structure, the authors found that the change in the work functions of phosphorene and graphene monolayers and hence the transition of the barrier from the n-type to the p-type are the result

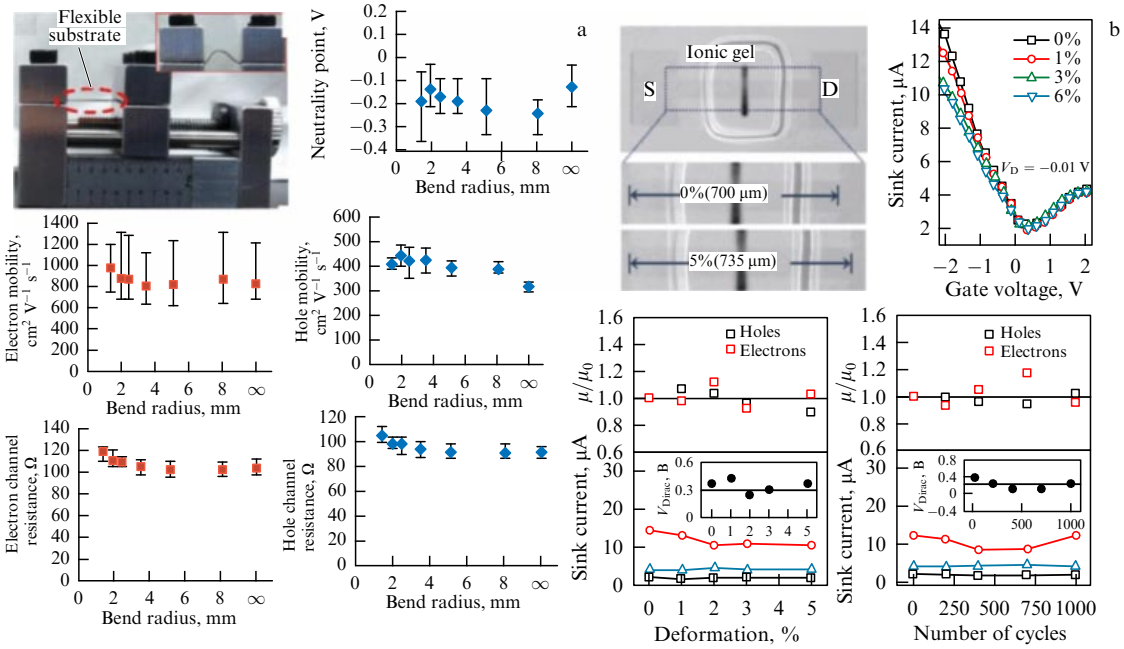

Figure 29. Dependence of the properties of a transistor with a graphene channel on the mechanical bending of the substrate. (a) Mechanical device for measuring bending and the dependence of the neutrality point stress, mobility, and contact resistances on the bending radius [246]. (b) Images of three-layer graphene FETs stretched by up to 5% along the channel and their typical performance at different deformations. Normalized hole and electron mobility, current levels, the minimum current at the neutrality point, and the Dirac point voltage as functions of the stretching level and during cycling under 3% stretching [247].

of a shift in the Fermi level in the phosphorene/graphene heterostructure under deformations in the structure plane. The possibility of tuning the electronic properties of phosphorene/graphene heterostructures using deformations presumably provides a basis for the development and manufacture of FETs and logic elements made of these materials.

Due to the high chemical activity of phosphorene, its structure is unstable against external influences. To protect chemically active 2D materials, heterostructures are often created from chemically active (inner layer) and chemically inactive (outer layer) 2D materials, such as graphene or boron nitride [241]. For phosphorene with graphene and boron nitride, the respective mismatch deformation is $\sim 1.8\%$ and $\sim 1.3\%$. The phosphorene/graphene heterostructure has a metallic nature, which is due to the graphene, while the phosphorene/h-BN heterostructure remains a direct-gap semiconductor, but its band gap increases significantly compared to the phosphorene monolayer: from 0.91 to 1.02 eV. An effective way to control the electronic properties of phosphorene/graphene or phosphorene/h-BN heterostructures is to change the distance d between layers, which governs the type of interatomic bonds. Changing d in the range of 2.50–4 Å (with the equilibrium value $d = 3.29$ Å) does not lead to the appearance of an energy band gap in the phosphorene/graphene heterostructure, but as d increases from 2.37 to 2.84 Å in the phosphorene/h-BN heterostructure, the band gap sharply increases from 0.91 to 1.23 eV; a further increase in d to 4 Å leads to a decrease in the band gap width to 0.95 eV, however. The interplanar distance can be changed experimentally using normal deformation.

Recently, a huge number of studies have appeared that demonstrate the possibility of creating various device structures from graphene and other 2D materials capable of operating under various types of deformations (see, e.g., [242–245]). In this review, as an example, we consider two options for FETs with a graphene channel. An FET with a gate 15 nm in thickness based on the Al_2O_3 dielectric with a high dielectric constant and an Si_3N_4 protective layer and with a graphene channel 30 nm in thickness was fabricated on a polyimide film (Fig. 29a [246]). The transistor had a channel length of 500 nm, maximum mobility of 800 $cm^2\ V^{-1}\ s^{-1}$, and operating frequency up to 100 GHz. The bending radius at which the transistor parameters change by no more than 20% was about 2 mm and corresponded to 4.6% stretching. Transistors in which channel and sink/source electrodes made of a graphene film without the use of traditional metal electrodes are shown in Fig. 29b [247]. The respective mobility of holes and electrons in these transistors was ~ 1200 and ~ 420 $cm^2\ V^{-1}\ s^{-1}$. The transistors operated stably without significant changes in their parameters when stretched up to 5%, even after 1000 or more deformation cycles. We note that stretching deformations of $\sim 5\%$ during the formation of transistors on organic films in many cases correspond to the bending of the film to a diameter of ~ 1 mm or less, i.e., almost double-folding. This provides a basis for using such transistors in foldable or wearable electronic devices.

8. Conclusion

Straintronics, as a platform for creating a new generation of information processing devices and the physical basis for the development of flexible electronics using 2D inorganic materials, is currently one of the most vigorously developing areas of nanoelectronics. The use of deformations can lead to surprising changes in the electronic properties of 2D materials and unexpected technological and engineering solutions. However, before straintronics can indeed be used, it must move further in its development. Because deformation is easier to control than, for example, the parameters of a potential barrier induced by the introduction of dielectric

elements into structures, the use of deformation offers an alternative approach to controlling various properties of 2D materials and designing unique structures based on them.

One widely discussed topic is the possibility of opening a band gap due to deformation in graphene or controlling the band gap in other 2D materials. For graphene, the band gap opening is theoretically predicted for deformations close to the maximum allowable one and for a combination of deformations of different types, primarily shear strains. Experimental data of this kind for graphene are practically absent, although this is a popular area of experimental work. The main experimental results on band gap control using deformations are related to transition-metal dichalcogenides (MoS_2, WS_2, etc.), graphene-like monolayer materials (black phosphorus, silicene, etc.), and heterostructures based on them. The ability to vary the band gap is very promising for optoelectronic and photovoltaic applications. In particular, local deformations allow creating a material with a spatially varying band gap (so-called 'funnels' or artificial atoms), which leads to selective collection of carriers in desired regions. This approach is promising for the development of photovoltaic cells. There are already methods for forming arrays of such artificial atoms by introducing arrays of locally deformed regions.

Among a range of interesting and important effects associated with deformations, we especially note the following.

(1) The theoretical and experimental dependences of the observed frequencies of Raman scattering peaks for various 2D materials turn out to be extremely sensitive to deformations and adsorption of atoms and molecules on the surface (in particular, to doping). This is a powerful tool for controlling the properties of nanostructures and searching for methods to control these properties. It is important that the locality of the Raman scattering method now reaches nanometers.

(2) The experimentally obtained coupling between layers in vdW heterostructures is typically quite large (0.7–1.0), which allows us to speak of various assembled heterostructures as a single whole. However, for a number of monolayers in a grown heterostructure, the possibility of their separation under deformations (slip effect) has been shown, as can be seen from Raman scattering. Such effects have been demonstrated for transition-metal dichalcogenides, giving rise to additional methods for creating modern nanoelectronic devices.

(3) The low mechanical strength of transition-metal dichalcogenides is a limitation for their practical use in flexible electronics. Important for applications is the fact that the heterostructures of transition-metal dichalcogenides and graphene, regardless of their assembly order, are mechanically more stable, mainly due to the mechanical reinforcement provided by the graphene layer. At the same time, it has been shown that the properties of heterostructures change significantly when the order of their assembly changes.

(4) Of particular interest is the possibility of local functionalization of materials and localization of foreign atoms or molecules with the introduction of nonuniform or local deformations. This opens broad prospects for the design of new nanomaterials and nanostructures. Deformations therefore play a key role in the design of nanostructures at the level of atoms, molecules, and monolayers, determining their final design.

Further progress in the development of straintronics can potentially pave the way for the development and creation of new functional elements of next-generation electronic and optoelectronic 2D devices. We especially note the significant predominance of theoretical studies over experimental ones. This is most likely due to the technological difficulties in creating certain structures and heterostructures based on monolayer materials.

Because 2D crystals can stretch more than bulk materials, the use of deformations can open the door to new applications of 2D materials and their unique properties. It is also worth mentioning that, although only electronic and optical properties are considered in this review, effects caused by deformations are also important for varying other properties, including magnetic ones [248]. Straintronics can be based on the piezoelectric properties of some families of 2D crystals, converting mechanical energy into electrical energy. For example, MoS_2, a material that is not piezoelectric in its bulk configuration, has been shown to become piezoelectric when thinned to a monolayer (or an odd number of layers) [249]. The authors controlled the conversion of mechanical energy into electrical energy and observed that the output voltage changed sign with a change in the direction of the applied deformation due to the lack of inversion symmetry in single-layer transition-metal dichalcogenides.

Effects that allow controlling the properties of known 2D materials and their heterostructures using deformation, and the development of new technological and engineering solutions for creating new structures are promising for specific electronic and optical applications, primarily for the development of flexible electronics based on inorganic materials. The use of straintronic approaches provides significant additional opportunities in the development of a vast range of everyday-life devices that people require, including all kinds of high-tech accessories, the Internet of things, smart clothes (wearable electronics), new-generation individual medical equipment, and much more. The relevance of the intensive development of flexible electronics is based on demand by society. Straintronics provides the physical and chemical foundations for the development of nanoelectronics of 2D materials and, in particular, flexible electronics, allowing the design of nanodevices that cannot be created by other methods.

Acknowledgments. This paper was supported by the Ministry of Science and Higher Education, grant 075-15-2020-797 (13.1902.21.0024).

References

1. Bukharaev A A et al. *Phys. Usp.* **61** 1175 (2018); *Usp. Fiz. Nauk* **188** 1288 (2018)
2. Sadovnikov A V et al. *Phys. Rev. Lett.* **120** 257203 (2018)
3. Barangi M, Mazumder P *Appl. Phys. Lett.* **104** 162403 (2014)
4. Arora A et al. *Phys. Rev. Mater.* **3** 024403 (2019)
5. Roy K *IEEE Trans. Nanotechnol.* **16** 333 (2017)
6. Roy K, Bandyopadhyay S, Atulasimha J *Appl. Phys. Lett.* **99** 063108 (2011)
7. Roy K *TechConnect Briefs* **4** 51 (2017)
8. Larionov K V, Sorokin P B *Phys. Usp.* **64** 28 (2021); *Usp. Fiz. Nauk* **191** 30 (2021)
9. Tsutsui G et al. *AIP Adv.* **9** 030701 (2019)
10. Lee M L et al. *J. Appl. Phys.* **97** 011101 (2005)
11. Susarla S et al. *ACS Nano* **12** 4036 (2018)
12. Wang D, Mei Y, Huang G *J. Semicond.* **39** 011002 (2018)
13. Cai P et al. *Adv. Mater.* **30** 1800572 (2018)

14. Ratnikov P V, Silin A P *Phys. Usp.* **61** 1139 (2018); *Usp. Fiz. Nauk* **188** 1249 (2018)
15. Antonova I V *Phys. Usp.* **60** 204 (2017); *Usp. Fiz. Nauk* **187** 220 (2017)
16. Heidari H, Wacker N, Dahiya R *Appl. Phys. Rev.* **4** 031101 (2017)
17. Carey T et al. *Nat. Commun.* **8** 1202 (2017)
18. Lee S et al. *Nat. Commun.* **8** 725 (2017)
19. Zhu W et al. *Flex. Print. Electron.* **2** 043001 (2017)
20. Zhao J, Zhang G-Y, Shi D-X *Chinese Phys. B* **22** 057701 (2013)
21. Liu Y, Pharr M, Salvatore G A *ACS Nano* **11** 9614 (2017)
22. Ameri S K et al. *ACS Nano* **11** 7634 (2017)
23. Popov V I et al. *Materials* **12** 3477 (2019)
24. Si C, Suna Z, Liu F *Nanoscale* **8** 3207 (2016)
25. Ni Z H et al. *Phys. Rev. B* **77** 115416 (2008)
26. Teague M L et al. *Nano Lett.* **9** 2542 (2009)
27. Zhang Y, Liu F *Appl. Phys. Lett.* **99** 241908 (2011)
28. Bronsgeest M S et al. *Nano Lett.* **15** 5098 (2015)
29. Sun G et al. *Nanotechnology* **20** 355701 (2009)
30. Huang M et al. *Proc. Natl. Acad. Sci. USA* **106** 7304 (2009)
31. Yu T et al. *J. Phys. Chem. C* **112** 12602 (2008)
32. Lee C et al. *Science* **321** 385 (2008)
33. Ding F et al. *Nano Lett.* **10** 3453 (2010)
34. Ferralis N, Maboudian R, Carraro C *Phys. Rev. Lett.* **101** 156801 (2008)
35. Yoon D, Son Y-W, Cheong H *Nano Lett.* **11** 3227 (2011)
36. Roldán R et al. *J. Phys. Condens. Matter* **27** 313201 (2015)
37. Deng S, Sumant A V, Berry V *Nano Today* **22** 14 (2018)
38. Politano A, Chiarello G *Nano Res.* **8** 1847 (2015)
39. Eletskii A V *Phys. Usp.* **50** 225 (2007); *Usp. Fiz. Nauk* **177** 233 (2007)
40. Cao G *Polymers* **6** 2404 (2014)
41. Galashev A E, Rakhmanova O R *Phys. Usp.* **57** 970 (2014); *Usp. Fiz. Nauk* **184** 1045 (2014)
42. Mortazavi B et al. *Comput. Mater. Sci.* **53** 298 (2012)
43. Wang G et al. *Phys. Rev. Let.* **123** 116101 (2019)
44. Knunyants I L (Ed.-in-Chief) *Khimicheskaya Entsiklopediya* (Chemical Encyclopedia) Vol. 1 (Moscow: Sov. Entsiklopediya, 1988) p. 608; http://www.nanoscopy.org/tutorial/graphite/graphite.html
45. Afanasov I M et al. *Inorganic Mater.* **45** 486 (2009); *Neorg. Mater.* **45** 540 (2009)
46. Georgakilas V et al. *Chem. Rev.* **112** 6156 (2012)
47. Shareena T P D *Nano-Micro Lett.* **10** 53 (2018)
48. Li X et al. *Appl. Phys. Rev.* **4** 021306 (2017)
49. Falin A et al. *Nat. Commun.* **8** 15815 (2017)
50. Lee K H et al. *Nano Lett.* **12** 714 (2012)
51. Petrone N et al. *ACS Nano* **9** 8953 (2015)
52. Clark N, Oikonomou A, Vijayaraghavan A *Phys. Status Solidi B* **250** 2672 (2013)
53. Gómez-Navarro C, Burghard M, Kern K *Nano Lett.* **8** 2045 (2008)
54. Nair R R et al. *Small* **6** 2877 (2010)
55. Cadelano E et al. *Phys. Rev. B* **82** 235414 (2010)
56. Peng Q, Ji W, De S *Comput. Mater. Sci.* **56** 11 (2012)
57. Li L H, Chen Y *Adv. Funct. Mater.* **26** 2594 (2016)
58. Li J, Medhekar N V, Shenoy V B *J. Phys. Chem. C* **117** 15842 (2013)
59. Liu K et al. *Nano Lett.* **14** 5097 (2014)
60. Antonova I V et al. *Mater. Design* **164** 107526 (2019)
61. Antonova I et al. *Materials* **13** 1032 (2020)
62. Antonova I V et al. *J. Material Sci. Eng.* **6** 1000379 (2017)
63. Ivanov A I et al. *Phys. Chem. Chem. Phys.* **19** 19010 (2017)
64. Young R J et al. *Compos. Sci. Technol.* **72** 1459 (2012)
65. Ni Z H et al. *ACS Nano* **2** 2301 (2008)
66. Mohiuddin T M G et al. *Phys. Rev. B* **79** 205433 (2009)
67. Yoon D, Son Y-W, Cheong H *Phys. Rev. Lett.* **106** 155502 (2011)
68. Huang M et al. *Nano Lett.* **10** 4074 (2010)
69. Mohr M, Maultzsch J, Thomsen C *Phys. Rev. B* **82** 201409 (2010)
70. Lee J E et al. *Nat. Commun.* **3** 1024 (2012)
71. Fiori G, Iannaccone G *Proc. IEEE* **101** 1653 (2013)
72. Kim M et al. *Nano Lett.* **10** 1125 (2010)
73. Fiori G et al. *Phys. Rev. B* **82** 153404 (2010)
74. Liu F, Ming P, Li J *Phys. Rev. B* **76** 064120 (2007)
75. Sahalianov I Yu et al. *J. Appl. Phys.* **126** 054302 (2019)
76. Choi S-M, Jhi S-H, Son Y-W *Nano Lett.* **10** 3486 (2010)
77. Farjam M, Rafii-Tabar H *Phys. Rev. B* **80** 167401 (2009)
78. Gui G, Li J, Zhong J *Phys. Rev. B* **78** 075435 (2008)
79. Gui G, Li J, Zhong J *Phys. Rev. B* **80** 167402 (2009)
80. Pereira V M, Castro Neto A H, Peres N M R *Phys. Rev. B* **80** 045401 (2009)
81. Ni Z H et al. *ACS Nano* **3** 483 (2009)
82. Li C-L *AIP Adv.* **4** 087119 (2014)
83. Cocco G, Cadelano E, Colombo L *Phys. Rev. B* **81** 241412 (2010)
84. Ramasubramaniam A, arXiv:1007.5511
85. Cocco G, Cadelano E, Colombo L, arXiv:1008.1238
86. Naumov I I, Bratkovsky A M *Phys. Rev. B* **84** 245444 (2011)
87. Choi S-M, Jhi S-H, Son Y-W *Phys. Rev. B* **81** 081407 (2010)
88. Gui G et al. *Appl. Phys. Lett.* **106** 053113 (2015)
89. Kerszberg N, Suryanarayana P *RSC Adv.* **5** 43810 (2015)
90. Souma S, Ohmi Y, Ogawa M *J. Comput. Electron.* **12** 170 (2013)
91. Alekseyev N I, Luchinin V V *RENSIT* **7** (2) 135 (2015)
92. He X et al. *Appl. Phys. Lett.* **104** 243108 (2014)
93. He X et al. *Appl. Phys. Lett.* **105** 083108 (2014)
94. McRae A C, Wei G, Champagne A R *Phys. Rev. Appl.* **11** 054019 (2019)
95. Si C et al. *Phys. Rev. Lett.* **111** 196802 (2013)
96. Tonnoir C et al. *Phys. Rev. Lett.* **111** 246805 (2013)
97. Ludbrook B M et al. *Proc. Natl. Acad. Sci. USA* **112** 11795 (2015)
98. Chapman J et al. *Sci. Rep.* **6** 23254 (2016)
99. Levy N et al. *Science* **329** 544 (2010)
100. Miller D L et al. *Science* **324** 924 (2009)
101. Betancur-Ocampo Y et al. *Ann. Physics* **359** 243 (2015)
102. Zhu S, Stroscio J A, Li T *Phys. Rev. Lett.* **115** 245501 (2015)
103. Zhang Y et al. *New J. Phys.* **13** 063047 (2011)
104. Pu H H et al. *Phys. Rev. B* **87** 085417 (2013)
105. Radchenko T et al., in *Nanooptics, Nanophotonics, Nanostructures, and Their Applications*: *Selected Proc. of the 5th Intern. Conf. Nanotechnology and Nanomaterials, NANO2017, August 23–26, 2017, Chernivtsi, Ukraine* (Springer Proc. in Physics, Vol. 210, Eds O Fesenko, L Yatsenko) (Cham: Springer, 2018) p. 25–41
106. Sagalianov I Yu et al. *Eur. Phys. J. B* **90** 112 (2017)
107. Guido Y Z, Ren V Z *Int. J. Numer. Model.* **31** e223 (2018)
108. Zhang X-W et al. *IEEE Electron Dev. Lett.* **36** 784 (2015)
109. Pang Y et al. *Adv. Sci.* **3** 1500419 (2016)
110. Kang M-A et al. *Carbon* **116** 167 (2017)
111. De Fazio D et al. *ACS Nano* **10** 8252 (2016)
112. Zhou R et al. *Materials* **10** 174 (2017)
113. Chhowalla M et al. *Nat. Chem.* **5** 263 (2013)
114. Gordon R A et al. *Phys. Rev. B* **65** 125407 (2002)
115. Jin Q et al. *J. Phys. Chem. C* **122** 28215 (2018)
116. Acerce M, Voiry D, Chhowal M *Nat. Nanotechnol.* **10** 313 (2015)
117. Lin Y-C et al. *Nat. Nanotechnol.* **9** 391 (2014)
118. Jiang J-W, Park H S *Appl. Phys. Lett.* **105** 033108 (2014)
119. Pang H et al. *Materials* **11** 502 (2018)
120. Mak K F et al. *Phys. Rev. Let.* **105** 136805 (2010)
121. Zhao W et al. *ACS Nano* **7** 791 (2013)
122. Manzeli S et al. *Nano Lett.* **15** 5330 (2015)
123. Feng J et al. *Nat. Photon.* **6** 866 (2012)
124. Castellanos-Gomez A et al. *Nano Lett.* **13** 5361 (2013)
125. He K et al. *Nano Lett.* **13** 2931 (2013)
126. Island J O et al. *Nanoscale* **8** 2589 (2016)
127. Conley H J et al. *Nano Lett.* **13** 3626 (2013)
128. Hui Y Y et al. *ACS Nano* **7** 7126 (2013)
129. Lloyd D et al. *Nano Lett.* **16** 5836 (2016)
130. Bandaru N et al. *J. Phys. Chem. C* **118** 3230 (2014)
131. Li H et al. *Nat. Commun.* **6** 7381 (2015)
132. Zhu T, Li J *MRS Bull.* **32** 151 (2007)
133. He X et al. *Appl. Phys. Lett.* **109** 173105 (2016)
134. Wang Y et al. *Nano Res.* **8** 2562 (2015)
135. Yang C, Zhao X, Wei S *Solid State Commun.* **245** 70 (2016)
136. Frisenda R et al. *npj 2D Mater. Appl.* **1** 10 (2017)
137. Amin B, Kaloni T P, Schwingenschlögl U *RSC Adv.* **4** 34561 (2014)
138. Li M, Daib J, Zeng X C *Nanoscale* **7** 15385 (2015)
139. Ghorbani-Asl M et al. *Phys. Rev. B* **87** 235434 (2013)
140. Guzman D M, Strachan A *J. Appl. Phys.* **115** 243701 (2014)
141. Johari P, Shenoy V B *ACS Nano* **6** 5449 (2012)
142. Yue Q et al. *Phys. Lett. A* **376** 1166 (2012)
143. Peelaers H, Van de Walle C G *Phys. Rev. B* **86** 241401 (2012)
144. Lu P et al. *Phys. Chem. Chem. Phys.* **14** 13035 (2012)
145. Scalise E et al. *Nano Res.* **5** 43 (2012)

146. Zhu C R et al. *Phys. Rev. B* **88** 121301 (2013)
147. Plechinger G et al. *2D Mater.* **2** 015006 (2015)
148. Yang S et al. *Nano Lett.* **15** 1660 (2015)
149. Gant P et al. *Mat. Today* **27** 8 (2019)
150. Liu C-C, Feng W, Yao Y *Phys. Rev. Lett.* **107** 076802 (2011)
151. Cai Y et al. *Phys. Rev. B* **88** 245408 (2013)
152. Mohan B, Kumar A, Ahluwalia P K *Physica E* **61** 40 (2014)
153. Wang Y, Ding Y *Solid State Commun.* **155** 6 (2013)
154. Çakr D, Sahin H, Peeters F M C M *Phys. Rev. B* **90** 205421 (2014)
155. Liu H et al. *ACS Nano* **8** 4033 (2014)
156. Rodin A S, Carvalho A, Castro Neto A H *Phys. Rev. Lett.* **112** 176801 (2014)
157. Peng X, Wei Q, Copple A *Phys. Rev. B* **90** 085402 (2014)
158. Fu D et al. *Appl. Phys. Lett.* **103** 183105 (2013)
159. Dai Z et al. *J. Mech. Phys. Solids* **137** 103843 (2020)
160. Zhang Y et al. *Nano Lett.* **18** 2098 (2018)
161. Zhang K, Arroyo M *Extreme Mechan. Lett.* **14** 23 (2017)
162. Pan W et al. *Sci. Rep.* **2** 893 (2012)
163. Dai Z, Liu L, Zhang Z *Adv. Mater.* **31** 1805417 (2019)
164. Sanchez D A et al. *Proc. Natl. Acad. Sci. USA* **115** 7884 (2018)
165. Li Z et al. *ACS Nano* **9** 3917 (2015)
166. Zhang K, Arroyo M *J. Mech. Phys. Solids* **72** 61 (2014)
167. Tsoukleri G et al. *Small* **5** 2397 (2009)
168. Dai Z et al. *Phys. Rev. Lett.* **121** 266101 (2018)
169. Kashyap J, Yang E-H, Datta D, arXiv:2001.00614
170. Panse K S, Zhou S, Zhang Y *ACS Appl. Nano Mater.* **2** 5779 (2019)
171. Castellanos-Gomez A et al. *Nano Lett.* **13** 5361 (2013)
172. Tyurnina A V et al. *ACS Photon.* **6** 516 (2019)
173. Li H et al. *Nat. Commun.* **6** 7381 (2015)
174. Chaves A et al. *npj 2D Mater. Appl.* **4** 29 (2020)
175. San-Jose P et al. *Phys. Rev. X* **6** 031046 (2016)
176. De Sanctis A et al. *Nat. Commun.* **9** 1652 (2018)
177. Zhai D, Sander N *Mod. Phys. Lett. B* **33** 1930001 (2019)
178. Cao Y et al. *Nature* **556** 80 (2018)
179. Cao Y et al. *Nature* **556** 43 (2018)
180. Settnes M, Garcia J H, Roche S *2D Mater.* **4** 031006 (2017)
181. Bi Z, Yuan N F Q, Fu L *Phys. Rev. B* **100** 035448 (2019)
182. Tong Q et al. *Nat. Phys.* **13** 356 (2017)
183. Liu J, Liu J, Dai X *Phys. Rev. B* **99** 155415 (2019)
184. San-Jose P, Gonźalez J, Guinea F *Phys. Rev. Lett.* **108** 216802 (2012)
185. Cao Y et al. *Phys. Rev. Lett.* **117** 116804 (2016)
186. Moon P, Koshino M *Phys. Rev. B* **85** 195458 (2012)
187. Gonzalez-Arraga L A et al. *Phys. Rev. Lett.* **119** 107201 (2017)
188. Saito Y et al. *Nat. Phys.* **16** 926 (2020)
189. Yan W et al. *Nat. Commun.* **4** 2159 (2013)
190. Huder L et al. *Phys. Rev. Let.* **120** 156405 (2018)
191. Chittari B L et al. *Electron. Struct.* **1** 015001 (2019)
192. Yankowitz M et al. *Nature* **557** 404 (2018)
193. Azadparvar M, Cheraghchi H, arXiv:1912.02017
194. Tang Q, Zhou Z, Chen Z *Nanoscale* **5** 4541 (2013)
195. Lehtinen P O et al. *Phys. Rev. Lett.* **91** 017202 (2003)
196. Elias D C et al. *Science* **323** 610 (2009)
197. Singh A K, Yakobson B I *Nano Lett.* **9** 1540 (2009)
198. Balog R et al. *Nat. Mater.* **9** 315 (2010)
199. Bae S-H et al. *Carbon* **51** 236 (2013)
200. Bao W et al. *Nat. Nanotechnol.* **4** 562 (2009)
201. Wang Z F, Zhang Y, Liu F *Phys. Rev. B* **83** 041403 (2011)
202. Zhang Y, Liu F *Appl. Phys. Lett.* **99** 241908 (2011)
203. Antonova I V, Nebogatikova N A, Prinz V Ya *J. Appl. Phys.* **119** 224302 (2016)
204. Nebogatikova N A et al. *Phys. Chem. Chem Phys.* **17** 13257 (2015)
205. Li T, Zhang Z *J. Phys. D* **43** 075303 (2010)
206. Wang Y et al. *ACS Nano* **5** 3645 (2011)
207. Zang J et al. *Nat. Mater.* **12** 321 (2013)
208. Hossain M Z et al. *Nat. Chem.* **4** 305 (2012)
209. Varchon F et al. *Phys. Rev. B* **77** 235412 (2008)
210. Hildebrand M et al. *J. Phys. Chem. C* **123** 4475 (2019)
211. Prinz V Ya et al. *Physica E* **6** 828 (2000)
212. Prinz V Ya *Physica E* **24** 54 (2004)
213. Prinz V Ya et al. *Sci. Technol. Adv. Mater.* **10** 034502 (2009)
214. Taziev R M, Prinz V Ya *Nanotechnology* **22** 305705 (2011)
215. Sorokin P B, Chernozatonskii L A *Phys. Usp.* **56** 105 (2013); *Usp. Fiz. Nauk* **183** 113 (2013)
216. Bertolazzi S, Brivio J, Kis A *ACS Nano* **5** 9703 (2011)
217. Castellanos-Gomez A et al. *Adv. Mater.* **24** 772 (2012)
218. Cooper R C et al. *Phys. Rev. B* **87** 035423 (2013)
219. Feldman J L *J. Phys. Chem. Solids* **37** 1141 (1976)
220. Kaplan-Ashiri I et al. *Proc. Natl. Acad. Sci. USA* **103** 523 (2006)
221. Elder R M, Neupane M R, Chantawansri T L *Appl. Phys. Let.* **107** 073101 (2015)
222. Lindahl N et al. *Nano Lett.* **12** 3526 (2012)
223. Zhong-can O-Y, Su Z-B, Wang C-L *Phys. Rev. Lett.* **78** 4055 (1997)
224. Jiang J-W et al. *Nanotechnology* **24** 435705 (2013)
225. Lee C et al. *Phys. Status Solidi B* **246** 2562 (2009)
226. Lin Y-C et al. *Nat. Nanotechnol.* **9** 391 (2014)
227. Chung J-Y et al. *J. Phys. D* **50** 345302 (2017)
228. Lin W et al. *Appl. Phys. Lett.* **114** 113103 (2019)
229. Sarwat S G et al. *Nano Lett.* **18** 2467 (2018)
230. Ghobadi N *Physica E* **111** 158 (2019)
231. Kretinin A V et al. *Nano Lett.* **14** 3270 (2014)
232. Liu X, Li Z *J. Phys. Chem. Lett.* **6** 3269 (2015)
233. Ye F, Lee J, Feng P X-L *Nanoscale* **9** 18208 (2017)
234. Lee I et al. *ACS Nano* **13** 8392 (2019)
235. Piccinini G et al. *2D Mater.* **7** 014002 (2020)
236. Amin B et al. *Appl. Phys. Lett.* **108** 063105 (2016)
237. Wei W, Dai Y, Huang B *Phys. Chem. Chem. Phys.* **19** 663 (2017)
238. Balendhran S et al. *Small* **11** 640 (2015)
239. Xiong W et al. *Nanotechnology* **28** 195702 (2017)
240. Liu B et al. *Phys. Chem. Chem. Phys.* **18** 19918 (2016)
241. Davletshin A R et al. *Physica B* **534** 63 (2018)
242. Heidari H, Wacker N, Dahiya R *Appl. Phys. Rev.* **4** 031101 (2017)
243. An J et al. *ACS Appl. Mater. Interfaces* **9** 44593 (2017)
244. Gupta S et al. *npj Flexible Electron.* **2** 8 (2018)
245. Jeerapan I, Poorahong S *J. Electrochem. Soc.* **167** 037573 (2020)
246. Lee J et al. *Appl. Phys. Lett.* **101** 252109 (2012)
247. Lee S-K et al. *Nano Lett.* **11** 4642 (2011)
248. Pan H *Sci. Rep.* **4** 7524 (2014)
249. Wang L, Wu M W *Phys. Lett. A* **378** 1336 (2014)